1-1-2007

Lunar surface: Dust dynamics and regolith mechanics

J. E. Colwell
University of Central Florida

S. Batiste

M. Horányi

S. Robertson

S. Sture

Recommended Citation

Showcase of Text, Archives, Research & Scholarship

LUNAR SURFACE: DUST DYNAMICS AND REGOLITH MECHANICS

J. E. Colwell,[1,2] S. Batiste,[3] M. Horányi,[3,4] S. Robertson,[4] and S. Sture[5]

[1] The lunar surface is characterized by a collisionally evolved regolith resulting from meteoroid bombardment. This lunar soil consists of highly angular particles in a broad, approximately power law size distribution, with impact-generated glasses. The regolith becomes densified and difficult to excavate when subjected to lunar quakes or, eventually, manned and unmanned activity on the surface. Solar radiation and the solar wind produce a plasma sheath near the lunar surface. Lunar grains acquire charge in this environment and can exhibit unusual behavior, including levitation and transport across the surface because of electric fields in the plasma sheath. The fine component of the lunar regolith contributes to the operational and health hazards posed to planned lunar expeditions. In this paper we discuss the mechanical response of the regolith to anticipated exploration activities and review the plasma environment near the lunar surface and the observations, models, and dynamics of charged lunar dust.

Citation: Colwell, J. E., S. Batiste, M. Horányi, S. Robertson, and S. Sture (2007), Lunar surface: Dust dynamics and regolith mechanics, *Rev. Geophys.*, *45*, RG2006, doi:10.1029/2005RG000184.

1. INTRODUCTION

[2] In this paper we review the mechanical properties of the lunar regolith and the interaction of the regolith with the lunar plasma environment. Lunar regolith is the layer of unconsolidated rocks, pebbles, and dust over primordial lunar bedrock. Broadly speaking, the entire lunar surface is regolith to a depth of at least several meters, and most of that is composed of small particles ground down by eons of meteoroid bombardment. It is on this thick global coating of dust, grains, and rock fragments that all manned and unmanned exploration on the Moon takes place. The Moon, like any object in a plasma, develops a surface charge, which, in turn, produces an electric field. The complex plasma environment immediately above the Moon's dusty surface varies over the course of the lunar day. Dust particles injected into this plasma from the regolith, either from human and mechanical activity or from meteoroid impacts or electrostatic forces, are affected by the electrostatic force as well as gravity while above the lunar surface, leading to unusual and time-variable dynamics. We first discuss the general properties of the lunar regolith, followed by a review of the physics of the charging of the lunar surface and the creation of a plasma sheath near the lunar surface. We review the evidence from past lunar missions for charged dust levitation and transport and experimental and theoretical studies of this process, which may be common to other dusty, airless objects in the solar system.

[3] The bedrock beneath the regolith includes, for example, the basalt deposits in the lunar mare dating to the time of mare formation some 3.8 billion years ago. The only process for producing regolith on the Moon is fragmentation by meteoroid impacts. The interplanetary meteoroid population at 1 AU roughly follows a power law size distribution, with a slight shallowing of the power law at micrometeoroids approximately $30-150$ μm in radius such that impactors of this size dominate the impacting mass flux [*Grün et al.*, 1985]. These micrometeoroids have a typical mass of about $10^{-10}-10^{-8}$ kg. They impact the lunar surface at speeds up to $\sim$72 km s^{-1}, delivering their kinetic energy to a point below the lunar surface at a depth comparable to the size of the impactor [*Holsapple*, 1993]. The yield, $Y = M_{\mathrm{ej}}/M_{\mathrm{imp}}$, from a hypervelocity impact (impact speed greater than the sound speed of the target material) can be anywhere from 10^3 to 10^6 depending on the target properties, where M_{ej} is the total ejecta mass created in an impact and M_{imp} is the impactor mass. Impacts into solid rock result in lower yields and higher ejecta velocities than impacts into unconsolidated sand or powder [*Housen et al.*, 1983; *Hartmann*, 1985; *Holsapple*, 1993]. Even for the lower range of values of Y it is clear that these impacts

[1]Department of Physics, University of Central Florida, Orlando, Florida, USA.
[2]Formerly at Laboratory for Atmospheric and Space Physics, University of Colorado, Boulder Colorado, USA.
[3]Laboratory for Atmospheric and Space Physics, University of Colorado, Boulder, Colorado, USA.
[4]Department of Physics, University of Colorado, Boulder, Colorado, USA.
[5]Department of Civil, Environmental, and Architectural Engineering, University of Colorado, Boulder, Colorado, USA.

TABLE 1. Definitions of Terms and Acronyms Used in This Paper

	Definition
Agglutinate	particle that is an aggregate of smaller soil particles bonded together by vesicular, flow-banded glass that is created by melting in micrometeoroid impacts.
ALSEP	Apollo Lunar Surface Experiment Package: a set of experiments deployed on the lunar surface by Apollo 17.
Anorthosite	igneous rock predominantly (>90%) composed of plagioclase feldspar.
AU	astronomical unit equal to semimajor axis of Earth's orbit or 1.49×10^8 km.
Basalt	hard, dark, volcanic rock composed primarily of plagioclase, pyroxene, and olivine.
Breccia	a coarse-grained rock produced in impact fragmentation composed of angular rock fragments held together by a mineral cement or a fine-grained matrix.
Dilation	volume change of a soil sample when loads are applied to that sample.
Dust	particles in the lunar regolith that can pass through a 100-μm sieve.
EASEP	Early Apollo Scientific Experiments Package: two experiments of known masses and pallet dimensions deployed on the lunar surface by Apollo 11.
Fines	particles in the lunar regolith that can pass through a 1-mm sieve.
HG	horizon glow: light observed at the western horizon after sunset by several Surveyor spacecraft cameras.
LEAM	Lunar Ejecta And Meteorites Experiment: part of the Apollo 17 ALSEP that detected impacts of charged dust particles levitated above the lunar surface.
LRV	lunar rover vehicle used in Apollo missions on the lunar surface.
Photoelectron layer	nonneutral layer of electrons over the sunlit lunar surface created by UV and X-ray production of photoelectrons from the lunar surface.
Plagioclase feldspar	aluminum-, calcium-, or sodium-rich silicate mineral, ranging from $NaAlSi_3O_8$ to $CaAl_2Si_2O_8$.
Plasma sheath	nonneutral layer at the physical boundary of a plasma where velocity differences between electrons and ions give rise to a potential gradient and an electric field.
Regolith	global layer of loose, unconsolidated particles, from boulders to dust, generated by meteoroid impacts.
Soil	particles in the lunar regolith that can pass through a 1-cm sieve.

produce ejecta particles that are much smaller than the impactor, resulting in a fine component of the lunar regolith.

[4] Less frequent larger impacts can penetrate the regolith and fragment the underlying bedrock producing the familiar large craters with rays of large ejecta blocks extending tens of impactor radii away from the crater. Beneath the fine-grained regolith that dominates the surface is a region of fractured blocks created by larger impactors. While this megaregolith is mainly composed of large-size particles, frequently in the range of 1 m or larger, the pore space between these large particles contains relatively fine material. The thickness of the mixture of the megaregolith and fine-grained regolith varies between 2 and 3 km. Contiguous and unfractured bedrock is located at depths greater than 10 km [*Hörz et al.*, 1977, 1991; *Hartmann*, 1980]. While the full size range of this impact-generated debris makes up the lunar regolith, we restrict our discussion in this paper to that part of the regolith smaller than 1 cm in diameter that has historically been called the lunar "soil" [*McKay et al.*, 1991]. Further classifying this component of the lunar regolith, we refer to the fraction that is smaller than 1 mm as "fines" and to the fraction that is smaller than 100 μm ($r = 50$ μm, where r refers to an effective particle radius) as "dust." Table 1 defines the terms and acronyms used in this paper, and Table 2 defines the symbols used.

[5] Lunar soil covers essentially the entire lunar surface to depths varying from a few meters to perhaps 15–20 m, interrupted by larger ejecta blocks and rocks. Generally, the regolith is deeper on the older highlands and less deep on the maria. The degree to which the soil has been compacted by impacts and lunar quakes can vary significantly across the lunar surface, and this compaction has consequences for engineering activities on the lunar surface. Because of the global coverage of the regolith and its relatively large depth, future manned and unmanned expeditions to the lunar surface as well as all foreseeable engineering activities will take place on and in the regolith. There are comprehensive reviews of the properties of the lunar regolith given by *McKay et al.* [1991], *Carrier et al.* [1991], *Papike et al.* [1991], and *Hörz et al.* [1991]; in section 2, we summarize those that are relevant for the processes discussed in this paper. In section 3 we describe the processes that charge the surface of the Moon, the near-surface plasma environment, and experimental and theoretical studies of plasma sheaths and photoelectron layers. In section 4 we discuss charging of lunar regolith particles and the effects of the electrostatic force on the dynamics of dust above the lunar surface. In section 4 we also review the observational evidence for charged dust levitation and transport over the lunar surface. We conclude by discussing the need for further theoretical, laboratory, and in situ investigations of the lunar regolith environment before long-duration manned expeditions to the Moon.

2. LUNAR REGOLITH

2.1. General Properties

[6] The six Apollo missions to land on the Moon returned 115 kg of lunar soil samples, and the Luna missions returned 321 g between 1970 and 1976. The mineralogy of these soil samples is discussed in detail by *McKay et al.* [1991], and the bulk mechanical properties are discussed by *Carrier et al.* [1991]. On a global scale the composition of the lunar regolith is distinguished by the dark basalts of the

TABLE 2. Definitions of Symbols

	Definition
c	cohesion (in units of stress) in a granular material (equation (2)).
c_s	sound speed in a plasma.
C_c, C_r	compression index, and recompression index, describing the degree to which a granular material compresses with increasing stress (equation (3)).
C_u	coefficient of uniformity for a soil sample, $C_u = d_{60}/d_{10}$, where d_{60} and d_{10} are defined the same way as d_{50}. A large value of C_u indicates a broad size distribution.
C_z	coefficient of curvature of a soil sample size distribution, $C_z = d_{30}^2/(d_{60} \times d_{10})$. A well-graded soil has $1 < C_z < 3$.
d_{50}	median particle size of a soil sample by weight. Fifty percent by weight of the particles will pass a sieve of this size.
d_{acc}	acceptable displacement of regolith subject to an overburden, in centimeters, at the 95% confidence level (equation (5)).
D_R	relative density of a granular material (equation (1)).
e	$e = n/(1 - n)$ is the void ratio in a granular material, where n is porosity (equation (1)); also, elementary electron charge.
ε_0	permittivity of free space.
ϕ	friction angle of a granular media (equation (2)).
Φ, Φ_d	plasma potential and dust particle potential (equations (8) and (16)).
G_S	specific gravity (density of a substance normalized to the density of water).
$I_{\mathrm{ph},0}$	photoelectron current from a surface exposed to solar UV.
k	Boltzmann constant.
K_0	coefficient of pressure, at rest, for a granular material (equation (4)).
λ_D	Debye length or characteristic shielding distance in a plasma (equation (12)).
n	porosity of a granular material (equation (1)); also, number density of electrons or ions in a plasma sheath (equations (6), (7), (10), (11), (18), and (19)).
q_{all}	allowable bearing capacity of a granular material for a given acceptable displacement (equation (5)).
σ', σ_h, σ_v	normal, horizontal, and vertical stresses, respectively (equations (2), (3), (4))
τ	shear stress in a granular medium (equation (2)).
T_e	electron kinetic temperature (equation (6)).
W	work function of a material (eV) (equation (17)).
z	vertical distance above the surface in a plasma or photoelectron sheath.

maria and the lighter-colored feldspar-rich rocks of the lunar highlands [*Vaniman et al.*, 1991a]. The bulk composition of the lunar soil varies between basaltic and anorthositic. More than a quarter of the lunar soil particles are agglutinates (fused soil), with a smaller fraction of impact-generated glasses and breccias. The distribution and properties of these compositional phases vary between the different sites that were investigated during the Apollo and Luna programs and depend highly on the geologic processes and mineralogy of the original material at the different locations [*Vaniman et al.*, 1991a]. In contrast to terrestrial soils the lunar regolith is relatively uniform in terms of composition and mineralogy because the mineral composition of the bedrock has far less variety: Fewer than a hundred distinct minerals have been found on the Moon as opposed to the many thousand minerals that exist on Earth [*Papike et al.*, 1991].

[7] While there can be significant variations in the relative abundance of the compositional phases (basalt, glasses, agglutinates, etc.) of the soil from place to place, the mechanical nature of the grains (primarily size distribution and shape or angularity) is derived from the impact process, which is essentially uniform across the Moon, although there are variations between the mare and the highlands. The steady bombardments of the lunar surface by charged subatomic and atomic particles from the Sun and stars have implanted gases and produced radionuclides, which, in addition to the bombardment history, distinguish lunar regolith particles from terrestrial rocks [*McKay et al.*, 1991]. Compositional variations are not large enough to significantly affect the response of the regolith to meteoroid impacts. However, there is some segregation of the lunar dust by composition, with the smallest particles consisting of a higher fraction of minerals that are more easily fragmented at small scales, such as plagioclase [*McKay et al.*, 1991]. In one sample, for example, the fraction of breccias and agglutinates declined from 59.5% in particles between 250 and 500 μm to 45.4% in particles between 20 and 45 μm, while the fraction of glasses and single-mineral grains such as plagioclase and pyroxene increased [*Houck*, 1982]. Compositional trends with particle size are summarized in Table 3 for another Apollo sample. Figures 1 and 2 show the cohesive fine-grained lunar regolith in images of the Surveyor 3 lander and the footprint it left in the regolith.

[8] Analyses of lunar soil samples, the spectra of the grains, and the spectral properties of different regions on the Moon have identified trends in the composition of the soil with maturity. The maturity of a soil is indicative of the amount of exposure to meteoroid bombardment and the solar wind and is therefore related to the age of the soil or, more precisely, the duration of its exposure at or near the surface. Microscopic analyses of soil samples have helped quantify maturity of soils through the abundance of nanophase iron as measured by the strength of ferromagnetic resonance intensity, I_S, relative to mafic iron, FeO [e.g.,

TABLE 3. Volume Abundances of Particles by Particle Size in Lunar Soil 15601,96[a]

	Size, μm						Sample
	250−500	150−250	90−150	75−90	45−75	20−45	Weighted Average
Weight percent	11.91	13.13	15.99	5.48	14.45	17.37	78.33
Single minerals[b]	21.4	35.4	39.7	53.3	47.6	52.5	41.5
Basalts	29.6	19.3	9.3	12.1	9.8	8.9	14.2
Breccias	5.7	6.1	4.9	5.6	6.2	4.7	5.5
Agglutinates	32.1	28.0	32.1	19.7	26.5	25.9	28.1
Glass	6.3	6.4	7.5	6.6	8.1	4.9	6.6
Number of particles	159	311	305	319	321	320	1735

[a]See *McKay et al.* [1991].
[b]Most single-mineral grains are plagioclase, pyroxene, and olivine. Abundances do not add up to 100% because unidentified and minor constituents are not listed. The weighted average for the whole sample is given in the right column.

McKay et al., 1991]. Recent studies of lunar soil maturity and variation between lunar samples and globally across the Moon, based on measurements of the optical properties and reflectance spectra from the Clementine spacecraft, are given by *Chambers et al.* [1995], *Taylor et al.* [1996], *Le Mouélic et al.* [2000], *Noble et al.* [2001], *Taylor et al.* [2001], and *Pieters et al.* [2006]. The maturity of a lunar soil is currently commonly defined by the ratio I_S/FeO, where the nanophase iron is in domains of ~10 nm within larger grains and is produced by reduction of FeO through impact processes. This index of maturity (as well as a number of other properties including mean and median particle sizes) is tabulated for all lunar samples by *Morris et al.* [1983]. Other indices that track maturity include grain size (decreases with increased bombardment) and implantation of nuclei from the solar wind, such as helium [*McKay et al.*, 1991]. Soils near the surface are generally more mature, reflecting their longer exposure to space weathering factors, and are also therefore typically smaller in mean size than particles deeper in the regolith.

2.2. Engineering Considerations

[9] Because the lunar surface is nearly entirely covered by unconsolidated regolith, this has been frequently invoked as a potential supply of raw materials for infrastructure, mineral resources, and fuel. When considering engineering involving the regolith, the significant differences between lunar and terrestrial soils due to differing geologic processes and overall environment should be considered. The lunar regolith particles, which are broken by bombardment, are much sharper than their terrestrial counterparts, and the agglutinates and spherical glasses, formed from impact, do not occur in the terrestrial environment. The sharper particles result in a much more abrasive material that requires special attention during the design of all equipment. In addition, the angular nature of the individual particles affects the bulk mechanics of the material, such as increasing interlocking between the angular and reentrant (locally concave) particles.

[10] In addition to the unusual regolith properties, characteristics of the lunar environment such as the high vacuum and absence of oxygen and water affect the surface properties of the individual grains and thus the bulk behavior. The decreased gravity on the lunar surface results in the

regolith existing at lower confining stresses than typically considered during terrestrial engineering, an effect which can significantly affect constitutive properties [*Sture et al.*, 2004]. The high vacuum can affect the surface cleanliness of particles and may result in a change of shear strength [*Perko et al.*, 2001]. Some of the engineering challenges and issues involved in utilizing and working with the lunar regolith are described by *Schrunk et al.* [1999]. *Lambe and Whitman* [1969] provide a review of basic soil mechanics.

[11] It is clear that the lunar regolith will behave differently than terrestrial soils in response to engineering activities. The extent of the differences is not fully understood because of the few opportunities to work with the regolith in situ, the unique particles that compose the regolith, and extreme environmental differences between the Moon and
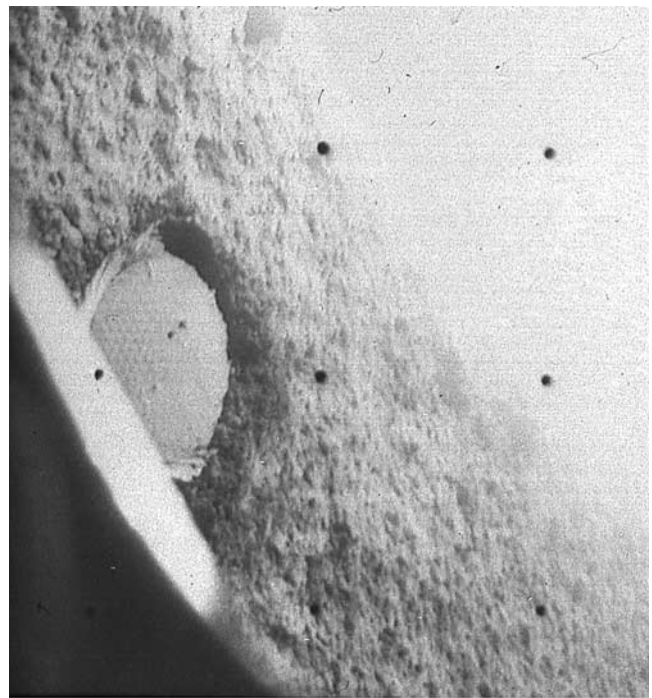

Figure 1. Surveyor 3 image of the footprint left by its own landing gear in the lunar regolith taken in April 1967. The waffle pattern of the landing gear is visible in the regolith revealing the fine nature of most of the regolith and its cohesive nature. Photograph from National Space Science Data Center.
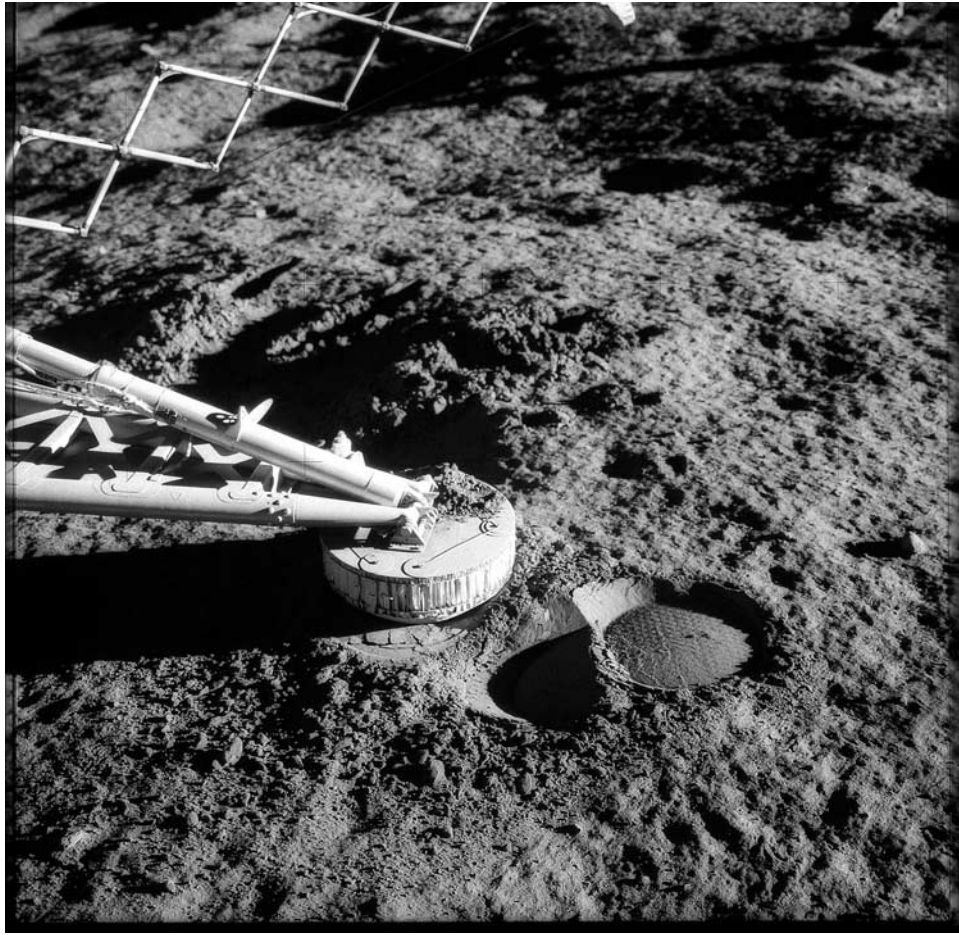
Figure 2. Apollo 12 photograph of the landing gear and scoop of the Surveyor 3 spacecraft taken 21 November 1969, 31 months after Surveyor 3 landed on the lunar surface. The pattern of the landing pad footprint imaged by Surveyor itself (Figure 1) is clearly visible and apparently unmodified in the intervening 31 months. Shallow trenches on the left dug by the Surveyor scoop demonstrate the ability of the regolith to support steep slopes. NASA photograph AS12-48-7110, Apollo 12 Principal Investigator Richard J. Allenby Jr., National Space Science Data Center.

Earth surfaces. However, prior research provides a great deal of information about the lunar surface and the regolith that will be invaluable for future exploration. Bulk properties of lunar samples have been measured, and such data can be used in design and planning for future missions. In addition to using measured properties of relatively small samples of lunar regolith, simulated materials have been developed to further support experimental research and improve our understanding of material properties for modeling and design.

2.2.1. Bulk Properties of Lunar Samples for Construction and Operation on the Lunar Surface

[12] The densities of individual lunar soil grains are typically $\sim$3 g cm^{-3} (specific gravity $G_S = 3$) with a porosity of the top 15 cm of $n \sim 0.5$ and a bulk density of 1.5 g cm^{-3} [*Mitchell et al.*, 1972a]. This seemingly high value for the porosity can be misleading because it includes pores within grains of complex shape. Estimates of the relative density of the lunar regolith, defined by

$$D_R = \frac{e_{max} - e}{e_{max} - e_{min}} \times 100\%, \qquad (1)$$

where $e = n/(1 - n)$ is the void ratio, n is the porosity, e_{max} is the maximum void ratio (least dense state) achievable, and e_{min} is the minimum void ratio (most dense state) achievable, exceed 60% at most locations. The relative density, which is quite low very near the surface, increases significantly just 10 cm below the surface to values exceeding the maximum relative densities achievable for terrestrial soils under normal construction conditions. These high values of D_R indicate that the lunar regolith is generally highly compacted. Tidal fluctuations between the Earth and Moon due to the Moon's eccentric orbit result in regular and continuous low-intensity seismic activity, which in addition to impacts of meteoroids have resulted in continuous densification of the regolith both at shallow and great depths [*Carrier et al.*, 1991]. In microgravity experiments a lunar regolith simulant with a relative density in excess of 50% produced virtually no ejecta when impacted at speeds of less than 1 m s^{-1}, while samples with lower relative densities produced abundant ejecta under the same conditions [*Colwell and Taylor*, 1999; *Colwell*, 2003]. An exception to the high relative densities of the lunar soil is

TABLE 4. Engineering Properties of Lunar Regolith[a]

Depth Range, cm	Average Bulk Density (± 0.05), g cm^{-3}	Void Ratio (± 0.07)	Relative Density (± 3), %	Average Cohesion, kPa	Average Friction Angle, deg
0–15	1.50	1.07	65	0.52	42
0–30	1.58	0.96	74	0.90	46
30–60	1.74	0.78	92	3.0	54
0–60	1.66	0.87	83	1.6	49

[a]Data are from *Carrier et al.* [1991], *Mitchell et al.* [1974], and *Houston et al.* [1974].

near crater rims where the relative densities can be less than 50%, suggesting that exploration activity in these areas may result in more dust leaving the surface as well as greater penetration into the soil by astronauts, vehicles, and equipment.

[13] In situ soil mechanics experiments were performed on Lunakhod 1 and 2 as well as at all Apollo landing sites. Various categories of hand-held, self-recording, and ad hoc penetrometers were used on all missions as the primary soil mechanics experiment. In addition, observations of Apollo activities resulted in both qualitative and semiquantitative data. The main sources of these data include (1) astronaut observations; (2) video and still images; (3) flight mechanics telemetry; (4) bearing of objects on the lunar surface (e.g., the Lunar Module, astronauts, Early Apollo Scientific Experiments Package, and hand tools); and (5) insertion of the contingency sampler handle, the solar wind composition experiment, the flagpole, and core tubes into the surface [*Sullivan*, 1994]. Laboratory testing of returned samples was also performed. In situ lunar regolith has been observed to be slightly more compressible than terrestrial lunar regolith simulants, which is believed to be due to the presence of easily crushed agglutinates [*Carrier et al.*, 1991]. The terrestrial experiments were performed on small samples at higher confining stresses than seen on the Moon. This results in lower measured shear strength because the interlocking of irregular particles that results in high strength at low pressures is either masked by high-pressure effects or does not take place at all because of the crushing of the fragile irregular agglutinates. Previous ground testing of lunar regolith has underestimated cohesion and friction angle described by the Mohr-Coulomb equation:

$$\tau = c + \sigma' \tan \phi, \qquad (2)$$

where τ is shear stress, c is cohesion, σ' is effective normal stress, and ϕ is the friction angle. In addition, the load-displacement behavior of regolith is highly nonlinear, with moduli dependent on confinement level and packing density [*Ko and Sture*, 1980] and friction dependent on surface properties, geometric dilatancy, and loading configuration (e.g., plane, uniaxial, and triaxial). In view of these considerations, in situ measurement data are more reliable [*Carrier et al.*, 1991]. Table 4 shows ranges for engineering properties of the in situ regolith, which to a large extent correspond to in situ regolith behavior. When densified, the strength of the regolith is quite high. This can make the

regolith difficult to excavate beyond the upper ~10 cm. This also serves to make the regolith more stable against disturbances from lunar quakes and nearby manned activity. The potential for a change in the engineering properties of processed regolith due to destruction of fragile agglutinate particles deserves attention.

[14] It is unknown whether the lunar regolith is normally consolidated or overconsolidated. Normally consolidated soils are compressed to a level in equilibrium with the load or overburden on the soil, while a soil can become over-consolidated if it is compressed by load and that load is later removed. Compressibility data, which describe the volume change, or densification, which occurs when a confining stress is applied to a soil, were obtained from ground testing of Apollo and Luna samples. For a normally consolidated regolith the compression index (C_c) ranges between 0.01 and 0.11 for dense regolith, where

$$C_c = -\frac{\Delta e}{\Delta \log \sigma_v}, \qquad (3)$$

where σ_v is the vertical stress. The recompression index, C_r (which is also given by equation (3), but the change is taken during recompression and not the initial compression), ranges between 0.000 and 0.013 [*Carrier et al.*, 1972, 1973; *Jaffe*, 1973]. These values are slightly higher than basaltic lunar simulant [*Carrier et al.*, 1972; *Mitchell et al.*, 1974]; the irregularly shaped particles, such as the agglutinates, break easily under low confining stress and also affect the porosity of the regolith, which, in turn, affects compressibility. The coefficient of pressure at rest,

$$K_0 = \frac{\sigma_h}{\sigma_v} \approx 1 - \sin \phi, \qquad (4)$$

where σ_h is the horizontal stress and ϕ is the friction angle [*Jaky*, 1944], has not been measured on the Moon. Assuming the regolith is normally consolidated, it is estimated to be in the range of 0.4–0.5, comparable to terrestrial sedimentary sand, and 0.7 if recompacted against the side of a structure or large immovable object.

[15] Ultimate bearing capacity or strength for applied surface loading, such as footprints, footings for habitat modules, and wheel-regolith contacts, is relatively high and typically in the range of 30–1800 kPa depending on the in situ regolith density. For practical engineering purposes the limit of applied loading is controlled by allowable settlements or displacements rather than bearing capacity,

except for loading applied to loose and medium-loose deposits that may exist near crater rims. On the basis of boot print analysis the allowable bearing capacity is given by [*Mitchell et al.*, 1974; *Carrier et al.*, 1991]

$$q_{all} = 2d_{acc} \text{kPa cm}^{-1}, \qquad (5)$$

where d_{acc} is the acceptable displacement for a 95% confidence level. For mobility purposes it is recommended that the contact pressure not exceed 1.4 kPa.

[16] At shallow depths (<30 cm), excavation or displacement of regolith will not pose a challenge. However, at increased depths the bulk density of the regolith increases, and with this the interlocking of particles, friction, and cohesion increase (Table 4). Excavation will become more difficult, as demonstrated during the Apollo 15 mission, when Astronaut Irwin reached a stiff layer at 30–35 cm that could not be penetrated with the scoop and required chipping to reach deeper levels [*Mitchell et al.*, 1972b]. While terrestrial methods exist to excavate or drill in difficult conditions, they often rely on large amounts of mass and energy and the ability to replace worn equipment. These resources, with the possible exception of electrical power, cannot be assumed to be abundant for lunar exploration. Novel approaches, such as relatively lightweight vibratory equipment to loosen interlocking regolith particles, will be required for soil processing [*Klosky et al.*, 1995, 1996; *Paterson*, 1992; *Szabo et al.*, 1998].

[17] Recompaction following excavation may occur both from human activities as well as shakedown compaction from lunar quakes. Undisturbed regolith, below the top 30 cm, is at or above 90% relative density. Following excavation, loosely piled regolith will be at 30–40% relative density, and machine compacting can achieve on the order of 65–75% relative density [*Carrier et al.*, 1991]. Because excavated regolith will not likely be as compact as the original undisturbed soil, designs must consider that the regolith will increase in volume by approximately 20% after excavation at depths greater than 0.5 m. In addition, it is possible that the lunar quakes will have an effect on geotechnical structures or cause settlement of structures if built on reprocessed regolith.

[18] A basic quantification of many mechanical properties of the lunar regolith has been performed. There are some unknowns because the material is certainly unique and the amount available for study is limited. However, there is sufficient information to begin planning and design that will meet the engineering challenges of the regolith and the lunar surface environment.

2.2.2. Lunar Regolith Simulants

[19] Because of the relatively limited supply of lunar soil samples and the destructive nature of standard engineering tests, lunar regolith simulants have been developed to better understand some of the bulk properties of lunar soil. The returned samples were studied to provide physical, chemical, and limited geotechnical properties, and that information was then used to select terrestrial soils that would sufficiently mimic the lunar regolith.

[20] During preparations for the Apollo missions, multiple lunar soil simulants were used for design and testing. Two such soils were Napa Valley Basalt (C_u = 33.0, d_{50} = 0.11 mm, G_s = 2.85, e_{max} = 1.116, and e_{min} = 0.360) [*Green and Melzer*, 1971] and Yuma Sand (C_u = 1.5, d_{50} = 0.12 mm, G_s = 2.67, e_{max} = 0.919, and e_{min} = 0.608) [*Freitag et al.*, 1970], both of which were utilized for the Lunar Roving Vehicle (LRV). Although the soils were not high-fidelity simulants, they facilitated development and successful operation of the LRVs.

[21] When new interest in lunar exploration arose in the late 1980s, new simulants were created that built upon the knowledge gained by Surveyor, Luna, and Apollo missions. One such simulant was created by researchers at the University of Minnesota, Minnesota Lunar Simulant 1 (MLS-1), from a basaltic rock with bulk chemistry resembling Apollo 11 mare soil sample 10084. MLS-1 contains less pyroxene than the Apollo 11 lunar mares, more feldspar, a small amount (<3% by volume) of biotite, surface ferric iron (3.5% by weight) in ilmenite and mafic silicates, 0.4% water, and surface oxidation [*Weiblen and Gordon*, 1988; *Weiblen et al.*, 1990]. The quarried basalt contains no glass or agglutinates, which made up the majority of sample 10084. While MLS-1 was a good mineralogical simulant, creating smaller particles and mixing soil for a representative particle-size gradation was left to individual researchers, perhaps limiting widespread use.

[22] MLS-1 was regraded by *Perkins* [1991] to represent the range of soil distributions collected by Apollo 11, 12, 14, and 15. A series of triaxial compression experiments were performed on MLS-1 and compared to lunar regolith data, with both sets of experiments performed in Earth's 1-*g* atmospheric environment (Tables 5a and 5b). The stiffnesses and softening behavior were comparable, indicating graded MLS-1 closely matches the strength and stiffness properties of lunar regolith. For two confining stress levels the results for friction angle are quite close; however, when examining the cohesion terms from direct shear experiments on MLS-1 with in situ regolith, the particle-assembly cohesion (or shear strength at zero confining stress) is low. This may be due to the lack of electrostatic charging and absence of agglutinate particles, which increase interlocking behavior [*Perkins*, 1991]. This simulant marked an improvement over the Apollo-era simulants.

[23] Prompted by the Space Exploration Initiative in 1989, a group of researchers convened a workshop to define requirements for a standard simulant to be used by the research community. The result was Johnson Space Center 1 (JSC-1), a low-titanium mare-like soil with a high percentage of glass. The soil was taken from a volcanic ash deposit near Flagstaff, Arizona, and sieved, and larger particles were crushed in an impact mill. The soil contained mainly plagioclase, pyroxene, and olivine but also a high percentage of (nonspherical) glass more closely matching a low-titanium mare soil [*Willman et al.*, 1995]. Large quantities of JSC-1 were produced, allowing distribution to several researchers. Major elements of JSC-1 include silicon oxide, aluminum oxide, and calcium oxide, making it

TABLE 5a. Lunar Regolith Simulants[a]

	Value	
	MLS-1	JSC-1
Percentage passing #200 sieve	43 [PM96]	36 [PM96]
C_u	16 [PM96]	7.5 [PM96]
C_c	1.1 [PM96]	1.12 [PM96]
d_{50}	$\approx$0.095 mm [PM96]	$\approx$0.11 mm [PM96]
G_S	3.2 [M94]	2.91 [W95]
e_{max}/ρ_{min}, g cm^{-3}	1.05/1.56 [PM96]	1.18/1.33 [PM96]
		—/1.43 [K2000]
e_{min}/ρ_{max}, g cm^{-3}	0.45/2.20 [PM96]	0.61/1.80 [PM96]
		—/1.83 [K2000]
Aspect ratio		0.68 [W95]
Glasses	no	yes
Agglutinates	no	no
Shear strength	$\phi = 58°$ for c = 0 at p = 10 kPa [PM96]	$\phi = 64°$ for $c = 0$ at $p = 10$ kPa [PM96]
		$\phi = 45°$; $c \leq 1$ kPa at $\rho = 1.5-1.65$ g cm^{-3} [M94]
		$\phi = 49°$; $c = 0.2$ kPa at $\rho = 1.9$ g cm^{-3} [P91]
		$\phi = 52-55°$; $c = 2.4-3.8$ kPa [C91]
		$\phi = 44.4°$; $c = 3.9$ kPa at $\rho = 1.62$ g cm^{-3} [K96]
		$\phi = 52.7°$; $c = 13.4$ kPa at $\rho = 1.72$ g cm^{-3} [K96]
Dilatancy angle		44.0° at $p = 1$ kPa and $\rho = 1.62$ g cm^{-3} [K96]
		40.5° at $p = 10$ kPa and $\rho = 1.62$ g cm^{-3} [K96]
		65.0° at $p = 10$ kPa and $\rho = 1.72$ g cm^{-3} [K96]
Residual strength	44° [PM96]	42° [PM96]
Young's modulus E, MPa	4.60 at $D_R = 37\%$ [P91]	18−60 at $D_R = 40\%$ [K2000]
	7.99 at $D_R = 66\%$ [P91]	65−110 at $D_R = 60\%$ [K2000]
	7.92 at $D_R = 97\%$ [P91]	(higher values are at higher stresses)
Bulk modulus K, MPa	$D_R = 37\%$ $K = 9.63$ MPa [P91]	$D_R = 40\%$, $K = 35-60$ [K2000]
	$D_R = 66\%$ $K = 7.69$ MPa [P91]	$D_R = 60\%$, $K = 75-110$ [K2000]
	$D_R = 97\%$ $K = 12.1$ MPa [P91]	(higher values are at higher stresses)

[a]Source abbreviations given within brackets are as follows: Cr70, *Cremers et al.* [1970]; C73, *Carrier et al.* [1973]; C91, *Carrier et al.* [1991]; C03, *Carrier* [2003]; J71, *Jaffe* [1971]; K96, *Klosky et al.* [1996]; K2000, *Klosky et al.* [2000]; M94, *McKay et al.* [1994]; P91, *Perkins* [1991]; PM96, *Perkins and Madson* [1996]; and W95, *Willman et al.* [1995].

comparable to MLS-1 and Apollo 14 lunar sample 14163 [*McKay et al.*, 1994]. Like MLS-1 it does not contain agglutinates that would increase material nonlinearities [*Perkins*, 1991]. JSC-1 is presently the industry standard lunar regolith simulant distributed widely for research and education.

[24] *Willman et al.* [1995] performed conventional triaxial tests on JSC-1 at 20.6, 34.4, and 68.7 kPa, equivalent to regolith at depths of 8−26 m. Specimens were prepared by tamping in three lifts, at densities of 1.50, 1.60, and 1.65 g cm^{-3}, ranging from 20 to 60% relative density. A

TABLE 5b. Lunar Regolith Samples

	Value
Percentage passing #200 sieve	52 [C03]
Cu	16 [C03]
Cc	1.2 [C03]
d_{50}	0.072 mm [C03]
G_S	2.9−3.2, 3.1 recommended [C91]
e_{max}/ρ_{min} (g cm^{-3})	1.39/1.26 (Apollo 11 [Cr70])
	—/1.15 (Apollo 12 [J71])
	2.26−2.37/0.87−0.89 (Apollo 14 [C73])
	1.94/1.10 (Apollo 15 [C73])
e_{min}/ρ_{min} (g cm^{-3})	0.67/1.80 (Apollo 11 [Cr70])
	—/1.93 (Apollo 12 [J71])
	0.87−0.94/1.55−1.51 (Apollo 14 [C73])
	0.71/— (Apollo 15 [C73])
Elongation	1.31−1.39 (Mahmood et al., unpublished report, 1974)
Aspect ratio	0.4−0.7 [*Görz et al.*, 1972]
Glasses	yes
Agglutinate	yes
Shear strength	$\phi = 30-50°$; c = 0.1−1.0 kPa [*Mitchell et al.*, 1974]
	$\phi = 42°$; $c = 0.52$ kPa at 0−15 cm depth [C91]
	$\phi = 46°$; $c = 0.90$ kPa at 0−30 cm depth [C91]
	$\phi = 54°$; $c = 3.0$ kPa at 30−60 cm depth [C91]
	$\phi = 49°$; $c = 1.6$ kPa at 0−60 cm depth [C91]

friction angle of 45° and cohesion of 1.0 kPa were reported for all densities, which is an unusual result: Strength is expected to vary with density as well as confining pressure.

[25] *Klosky et al.* [1996, 2000] performed multiple triaxial tests of JSC-1 at pressures ranging from 1 to 80 kPa with samples prepared using base vibration at three density levels (1.62, 1.71, and 1.81 g cm^{-3}) corresponding to 53, 75, and 95% relative density (Tables 5a and 5b). The material shows high friction angles and apparent cohesion, as does lunar regolith. In addition to verifying that the mechanical characteristics of the material were an appropriate simulation of lunar regolith, *Klosky et al.* [2000] also demonstrated the importance of the environment in which the material exists. The increasing trend in dilatancy angle with decreasing confining stress supports the Klosky et al. observation that the Mohr-Coulomb model used to determine friction angle and cohesion showed nonlinearity at low pressures. That is, constitutive behavior, or the way the soil contracts and expands under loading and unloading, is dependent on the confining stress on the material, particularly at low confining stress. With the reduced gravity on the Moon it is therefore particularly important that the confining stress be considered when determining load conditions for construction on and in lunar regolith.

[26] Currently, little of the MLS-1 or JSC-1 simulants remain in distribution, however, and limited quantities of other simulants, such as the Japanese FJS-1 and MKS-1, are available. To provide a large quantity for wide distribution, production of a new lunar soil simulant in the United States is underway with the support of NASA. Internationally, several other businesses and organizations are also producing simulants. Simulants offer the opportunity to allow extensive experimental testing as the quantity available is much greater than lunar regolith. It can be used to provide test beds for various exploration activities and equipment designs as well as model verification. While an important asset, the ability to simulate the lunar environment should be evaluated carefully. Simulants do differ from the lunar regolith (particle shapes, mineralogical composition, size distribution to varying degrees), and it is important to be aware of those differences in relation to how the simulant is to be used. For instance, for geotechnical engineering the detailed chemical composition is not as important as the grain shape or size distribution. For chemical processing, though, the composition may be more important. The goodness of a simulant has to be examined on a case-by-case basis. Also, the simulant (and lunar regolith) behavior is dependent on temperature, gravity, vacuum, etc., conditions of the environment in which it is used; to be most effective, the environment should be simulated as closely as possible. Where that is not feasible, the limitations of simulating the lunar environment on Earth should be taken into account when extrapolating to the Moon.

2.3. Electrostatic Considerations

[27] The relative strength of the electric force on lunar dust particles depends on the ratio of surface area to mass, or specific surface area, which is a function of the shape of the grains. On the basis of laboratory measurements of lunar soil samples, lunar soil has been characterized as a well-graded (or poorly sorted, meaning a smooth and continuous size distribution) granular material with the majority of particles in the 45- to 100-μm size range. In contrast to terrestrial soils, which have typically undergone complex and continuous erosional, degradation, and transport processes that result in generally rounded, subrounded, or slightly angular shapes, the majority of lunar regolith is highly angular and elongated in shape [*Heywood*, 1971; *Görz et al.*, 1971, 1972; *Carrier et al.*, 1991; A. Mahmood et al., Particle shapes of three lunar soil samples, unpublished report, available from W. D. Carrier III, 1974, hereinafter referred to as Mahmood et al., unpublished report, 1974]. The integrated specific surface area for a lunar soil sample, including the full distribution of particle sizes, is equivalent to a collection of spherical particles with a radius $r = 2$ μm, far smaller than the mean or median particle size [*Carrier et al.*, 1991]. A more telling parameter is the ratio of the specific surface area for lunar soil to a sample of spheres with the same size distribution. This equivalent surface area ratio is nearly a factor 8 for lunar soil samples, reflecting the angular, complex shapes of most of the particles [*Cadenhead et al.*, 1977; *Carrier et al.*, 1991].

[28] The size distribution of the lunar regolith varies to some extent with location and with soil maturity. The mean sizes of most lunar soil samples are between 45 and 100 μm, but the size distribution is broad with $\sim$20% by mass of the soil smaller than 20 μm [*McKay et al.*, 1991; *Carrier et al.*, 1991]. It is this smallest component of the lunar regolith size distribution that is susceptible to electrostatic forces because of their higher charge-to-mass ratios.

3. LUNAR SURFACE CHARGING AND ELECTRIC FIELDS

[29] Dust charging in space plasmas includes a number of complex processes, including the collection of electrons and ions, photoemission, secondary electrons, and thermionic and field emission of electrons. The composition and energy distribution of the plasma and the intensity of the electromagnetic radiation as well as the size, composition, and surface properties of the dust grains influence the charge state of a dust particle. In addition, the presence of neutrals might influence dust charging as well. The physics issues for charging in space and dusty plasma physics were initially reviewed by *Whipple* [1981] and *Goertz* [1989], respectively. A series of conferences on dusty plasmas [e.g., *Bharuthram et al.*, 2002; *Thomas et al.*, 2004] have resulted in conference proceeding volumes that review more recent developments. On the lit lunar surface outside the geotail the collection of solar wind electrons and ions and solar UV-induced photoemission are thought to be the most important charging currents. On the dark side of the Moon, especially inside the geotail, streaming ions and a hot plasma population, respectively, can further complicate the charging environment. A number of important early works on the

basic physics of lunar charging and observations from Apollo and earlier unmanned lunar missions are given by *Grard* [1973]. An review of the Apollo data and theoretical studies of the lunar surface potential, near-surface plasma environment, and associated electric fields is given by *Freeman and Ibrahim* [1975]. Here we review the surface potential of the Moon and the resulting plasma conditions and electric fields near the lunar surface, which can affect the behavior of dust above the lunar surface. Dust may leave the surface because of perturbations from human or robot activity, meteoroid impact, or electrostatic forces as described in section 4.

3.1. Lunar Surface Potential

[30] The lunar surface is subjected to a number of currents that can vary over the course of a lunar day [*Manka*, 1973]. A patch of the lunar surface will reach a charge such that the currents to and from the surface have a sum of zero. The Moon is immersed in the solar wind, a plasma with a variable speed composed primarily of protons and electrons. Because of the faster speed of the thermal electrons the surface would collect electrons and charge negative in the absence of other currents, and the surface potential in volts would be on the order of the electron energy in eV. The lunar surface is also directly exposed to the full solar spectrum including high-energy photons that can eject electrons from the surface. If this photoemission is the dominant current, then the surface loses electrons and becomes positively charged to a surface potential approximately equal to the energy of the photoelectrons.

[31] Electrons can also be emitted by the impact of a particularly energetic charged particle such as energetic electrons in the Earth's magnetotail. The yield of these secondary electrons can exceed unity for primary electron energies >100 eV, and these secondary electrons then become an important current in determining the equilibrium potential of the surface [*Horányi et al.*, 1998]. We will restrict ourselves to photoemission and solar wind currents for much of the following discussion; although when the Moon is in the Earth's plasma sheet, the secondary electron current may dominate these other effects and give rise to much larger surface charges and stronger electric fields [*Halekas et al.*, 2005].

[32] On the dayside of the Moon the charging is dominated by photoemission from solar ultraviolet and soft X-ray photons, while the nightside surface charge is determined by a balance between collection of solar wind protons and electrons. A typical flow speed for the solar wind is ~400 km s^{-1}, and a typical temperature of the solar wind plasma is 10 eV, well below the energy range where secondary electron production becomes important. The solar wind temperature corresponds to a typical thermal speed of ~44 km s^{-1} for the protons and 1900 km s^{-1} for the electrons, with the difference due to the smaller mass of the electrons. Consequently, a void in the solar wind protons behind the Moon starts to form. However, as electrons try to leave behind the protons, a polarization electric field will build up, accelerating the ions and slowing the electrons,

resulting in a filling of the plasma void behind the Moon. The lunar wake is often modeled as a plasma expansion into vacuum [*Samir et al.*, 1983]. This expansion leads to enhanced electron temperatures and streaming ion beams toward the surface [*Halekas et al.*, 2005]. Measurements of electrons on the lunar nightside by the Lunar Prospector spacecraft support this simple model and suggest a nightside lunar surface potential of at least −35 V and more likely near −100 V [*Halekas et al.*, 2002]. In the Earth's magnetotail the potential is negative, and the absolute value may exceed −500 V at times because of high-energy electron fluxes to the surface, usually within the Earth's plasma sheet [*Halekas et al.*, 2005]. These large negative surface potentials, inferred from Lunar Prospector data, occurred most frequently on the lunar nightside but were also observed on the dayside when the photoelectron current would be expected to prevent such large negative potentials. *Halekas et al.* [2005] interpret this as evidence for strong variability in the photoelectron current from the lunar surface, which, in turn, suggests the possibility of small-scale spatial and temporal variations in the dayside lunar surface potential.

[33] Values for the lunar surface potential were also obtained by the Apollo Suprathermal Ion Detector Experiment. This instrument found the energy of ions at the lunar surface and determined the dayside potential to be about +10 V [*Freeman and Ibrahim*, 1975]. Data from the Apollo 14 Charged Particle Lunar Environment Experiment (CPLEE) with upward looking apertures 26 cm above the lunar surface detected photoelectrons on the lunar dayside with energies up to 200 eV when the Moon was in the Earth's magnetotail. Because the photoelectrons emitted from the surface of the Moon have at most an energy of a few eV (section 3.2), these high-energy electrons must have been accelerated to the surface by a positive surface potential of about 200 V [*Reasoner and Burke*, 1973]. These high potentials are reached when the Moon is in the Earth's magnetotail and shielded from the solar wind: Outside of the magnetotail, solar wind electrons partially neutralize the effects of photoemission and result in the lower surface potential of about +10 V. The height dependence of the electric field resulting from the surface charge density depends on the plasma density above the surface. Hence stronger electric fields are expected on the lit side pointing away from the Moon than on the nightside pointing toward the surface.

[34] The potential at the terminator was determined to be about −70 V with the transition from the positive dayside potential to negative potentials occurring on the lit side of the terminator where the incidence angle of solar photons declines but the fast thermal electrons still have direct access to the surface [*Freeman and Ibrahim*, 1975]. The terminator region has a complicated potential because of the reduction in photoemission at low solar zenith angles on large spatial scales together with the presence of shadows adjacent to more directly illuminated and photoemitting surfaces on the small spatial scale of boulders, rocks, and crater rims. This could produce strong localized electric fields because of the variation in the photoelectron current
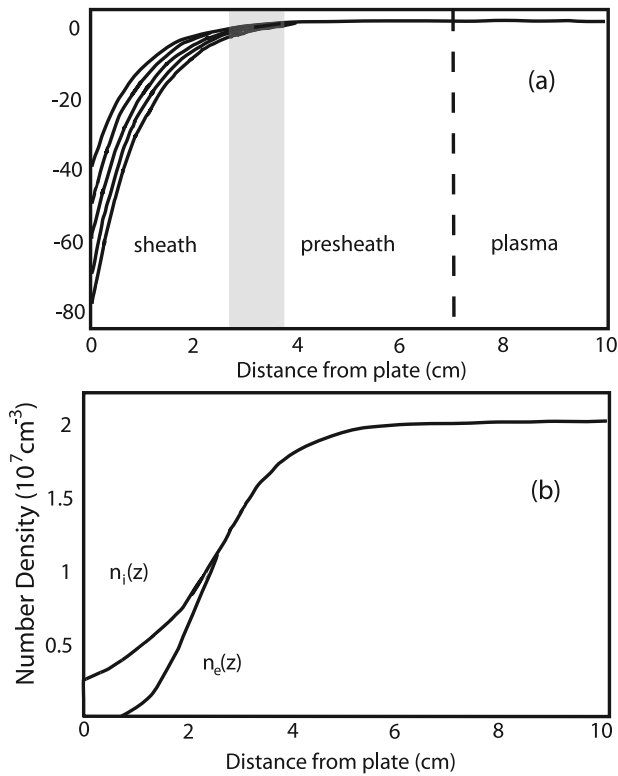
Figure 3. (a) Measured plasma sheath potential profiles as a function of distance from the surface, $\phi(z)$. Curves represent sheath profiles for five different surface potentials ranging from ~40 V to ~80 V obtained by least squares fits to data using the sheath profile given in equation (8). The gray rectangle denotes the range of distances from the plate at which $\phi = 0$ V for each surface bias. The inner edge of the rectangle corresponds to the sheath extent for V_b = ~40 V, while the outer edge is the sheath extent for V_b = ~80 V. (b) Electron and ion densities are found using equations (6) and (7), respectively, for a surface biased to ~40 V. From *Sickafoose et al.* [2002].

from shadowed to illuminated regions. The terminator region is further complicated by the difference in the shadowing of solar photons and solar wind protons. The latter are aberrated by the Moon's velocity around the Sun and so arrive from a direction $V_{\text{Moon}}/V_{SW} \approx 4°$ away from the solar direction, where V_{Moon} and V_{SW} are the speed of the Moon around the Sun and the solar wind speed, respectively. At the dawn terminator, there is a region 4° in longitude (at the Moon's equator) that experiences the solar wind proton flux but no photoemission, and at the dusk terminator, there is a similar region that is illuminated by the Sun but is screened from the incoming solar wind protons. The time for the Sun to rise or set past this 4° terminator transition region (at the lunar equator) is approximately 8 hours.

[35] In sections 3.2 and 3.3 we summarize the expected properties of the plasma layer above the lunar surface. At night the subsonic electron flux remains constant while the supersonic ion flow initially forms a cavity. This leads to a negative surface charge density distribution. An electric field is generated that points toward the surface. This accelerates ions toward the surface with the consequence

that ion and electron fluxes to the surface are equalized. The plasma sheath above the surface is dominated by ions (section 3.2). During the day, photoelectrons are emitted, and the surface charge density becomes positive. The electric field generated in this case points away from the surface returning the photoelectrons. The sheath above the surface in this case is dominated by electrons (section 3.3). In the geotail, where a local hot plasma population influences the surface potential, models of surface charging are less secure, and more in situ measurements are needed.

3.2. Plasma Sheath

[36] On the nightside the surface charge leads to a non-neutral layer above the lunar surface called a Debye, or plasma, sheath. Above the plasma sheath the plasma is neutral, while within the sheath the separation of charge induced by the negative charge on the surface results in a gradient in the charge density. This gradient then leads to an electric field near the surface and directed toward the surface such that positively charged ions are accelerated toward the surface. Plasma sheath profiles and electric fields have been extensively studied. Recent analyses are given by *Riemann* [1995, 1997].

[37] *Sickafoose et al.* [2002] examined the charging of dust grains in a plasma sheath for studies of dust levitation. The electrons within the plasma sheath can be assumed to have a Maxwellian velocity distribution,

$$n_e(z) = n_0 \exp\left[\frac{e\Phi(z)}{kT_e}\right], \qquad (6)$$

where n_0 is the density in the neutral plasma beyond the sheath, $\Phi(z)$ is the height-dependent potential within the sheath, z is vertical distance above the surface in a plasma sheath, k is the Boltzmann constant, and T_e is the electron temperature. Ions are accelerated by the potential gradient at the sheath-plasma boundary to the sound speed, $c_s = \sqrt{kT_e/m_i}$, where m_i is the ion mass [*Bohm*, 1949; *Lieberman and Lichtenberg*, 1994]. Ions are accelerated to this velocity when the potential drop is $kT_e/2$. This defines the sheath edge, and at this point the ion and electron densities are $n_{i,e}(\text{edge}) = \exp(-1/2)n_0$ [*Sickafoose et al.*, 2002]. The ion density in the sheath can then be determined from the continuity equation and is

$$n_i(z) = n_i(\text{edge})\left[1 - \frac{2e\Phi(z)}{m_i c_s^2}\right]^{-1/2}. \qquad (7)$$

[38] Laboratory measurements of plasma sheaths show sheath potentials relative to the plasma potential described by an exponential,

$$\Phi(z) = -\Phi_0 e^{-bz}, \qquad (8)$$

where Φ_0 is the potential bias of the surface, such as the lunar surface potential, and b is the inverse scale height [*Arnas et al.*, 1999, 2000, 2001; *Sickafoose et al.*, 2002]. The electric field within the sheath therefore also falls off exponentially with distance from the surface. Measured sheath potential profiles and derived ion and electron densities are shown in Figure 3.

[39] Dust loading of the sheath could have a strong effect on the sheath itself if the charge density locked up in grains above the surface becomes comparable to the electron density, for example. Over a positive surface charge density the sheath is electron-rich, and the electric field points away from the surface. Therefore at heights where photoemission from a grain overcomes its own electron collection from the sheath, dust particles will charge positively. In this case the electric force can balance gravity, and grains can be stably levitated. The height where this occurs depends on the electric field as well as the size and density of the dust grain (section 4.4). As more and more particles are loaded into the sheath, their charges are reduced, and the potential distribution is vertically stretched, so larger particles can no longer be stably levitated. There is thus a tendency for the dust density to be self-regulating and for there to be a natural upper limit of grain size in levitated dust clouds above the lunar surface [*Nitter et al.*, 1994, 1998].

3.3. Photoelectron Layer

[40] On the dayside both solar wind protons and electrons strike the surface, but the additional current produced by photoemission of electrons results in a positively charged daytime surface as described in section 3.2. Photoelectrons return to the surface in response to the positive charge created by photoemission. Just as the negatively charged surface produces a plasma sheath over the nightside of the Moon, the photoelectrons lead to a nonneutral layer over the dayside surface called a photoelectron layer or photoelectron sheath. The photoelectron sheath is a region of excess electrons unlike the plasma sheath, which is a layer where the electron density is less than the ion density. The electric field within the photoelectron layer is directed away from the surface such that the electrons are accelerated toward the surface and positively charged particles experience an upward electric force.

[41] The sheath profile depends on the energy distribution of the photoelectrons, which, in turn, depends on the spectrum of the incoming radiation and the work function of the surface. Characteristics of photoelectron sheaths were studied in several papers in connection with the initial exploration of the lunar surface [*Singer and Walker*, 1962; *Grard and Tunaley*, 1971; *Tunaley and Jones*, 1973; *Walbridge*, 1973].

[42] The photoelectron density in the sheath is determined by the photoelectron current away from the surface and the resulting positive surface potential. The photoelectron current is determined by the flux of solar photons with sufficient energy to knock electrons off the surface, $F(\lambda < \lambda_{crit})$, and the quantum efficiency of photoemission from the material, $\chi(\lambda)$:

$$I_{ph0} = \int_0^{\lambda_{crit}} F(\lambda)\chi(\lambda)d\lambda, \qquad (9)$$

where $\lambda_{crit} \sim 250$ nm is the longest-wavelength photon capable of producing a photoelectron from a surface with a typical work function, $W \sim 5$eV [e.g., *Sternovsky et al.*,

2002]. The photoemission efficiency, $\chi(\lambda)$, has been directly measured for lunar regolith samples taken by Apollo 14 and Apollo 15, and the resulting photocurrent is $I_{ph0} = 2.8 \times 10^9$ electrons cm^{-2} s^{-1} [*Willis et al.*, 1973]. This is roughly one tenth of the photocurrent from a metal in the solar flux [*Manka*, 1973]. *Reasoner and Burke* [1973] adopt $\chi = 0.1$ for $\lambda < 138$ nm and $\chi \propto E_{ph} - W$ for 138 nm $< \lambda < 200$ nm, where E_{ph} is the photon energy, based on the CPLEE data. The photoelectron density at the surface is given by [*Colwell et al.*, 2005]

$$n_{pe,0} = 2I_{ph0}\sin(i_s)/\upsilon_{pe}, \qquad (10)$$

where υ_{pe} is a characteristic photoelectron emission velocity, i_s is the solar elevation angle above the horizon, and the factor of 2 accounts for the upward and downward flux of electrons. *Willis et al.* [1973] have an additional factor of $\sqrt{\pi}$ in their expression for $n_{pe,0}$, which is based on energy arguments rather than flux.

[43] The photoelectron energy distribution measured by *Willis et al.* [1973] is narrower than a Maxwellian because there is a relatively low upper limit to the photoelectron energy set by the energy difference of the most energetic solar photons and the surface work function. Solar Lyman α photons produce photoelectrons with an energy of about 4 eV if the lunar surface work function is 6 eV [*Reasoner and Burke*, 1973]. The observed photoelectron energy distribution peaks at $\Phi_{pe} = 2.2$ eV and extends to energies of about 6 eV [*Willis et al.*, 1973]. The peak of the distribution corresponds to a photoelectron velocity, $\upsilon_{pe} = 8.8 \times 10^7$ cm s^{-1}, which from equation (10) gives a photoelectron density at the surface of $n_{pe,0} \sim 60$ cm^{-3}.

[44] For relatively low photoelectron energies a Maxwellian distribution is a reasonable approximation to the measured photoelectron energies. In this case the photoelectron density in the sheath as a function of height above the surface can be derived analytically and is given by [*Grard and Tunaley*, 1971]

$$n_{pe} = n_{pe,0}\left(1 + \frac{z}{\sqrt{2}\lambda_D}\right)^{-2}, \qquad (11)$$

where z is the height of the grain above the surface and

$$\lambda_D = \sqrt{\frac{\varepsilon_0 \Phi_{pe}}{4\pi n_{pe,0}e}}, \qquad (12)$$

with Φ_{pe} in eV and where ε_0 is the permittivity of free space and λ_D is an effective Debye length at the surface for the photoelectrons. Using the maximum photoelectron energy of $\Phi_{pe} = 6$ eV and a relatively tenuous photoelectron density at the surface of $n_{pe,0} \sim 60$ cm^{-3}, the Debye length at the surface is $\lambda_D \approx 66$ cm.

[45] More detailed solutions of the charge distribution, including particle-in-cell calculations [*Sickafoose et al.*, 2001] and solutions of Poisson's equation including photoelectron and plasma populations [*Nitter et al.*, 1998] give a vertical profile similar to that in equation (11). *Reasoner*
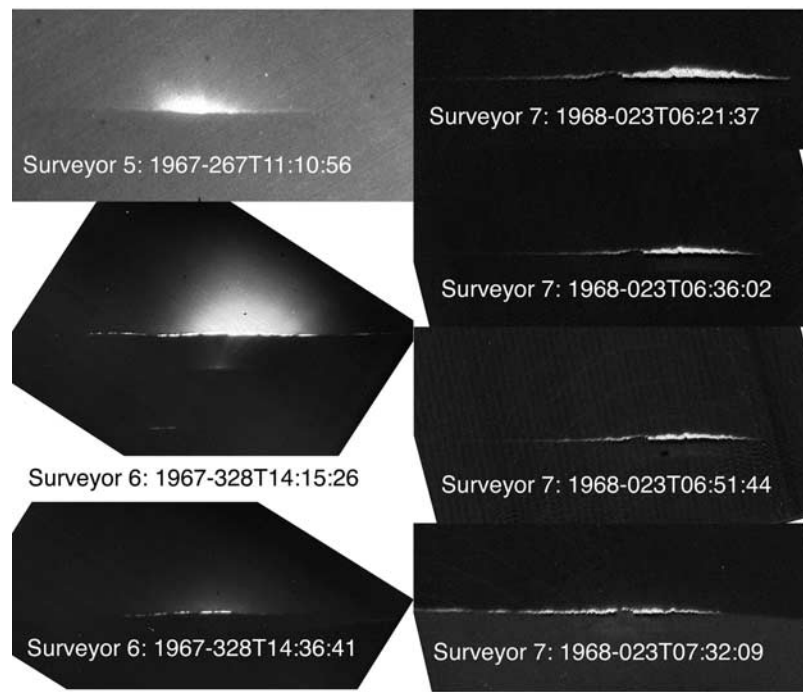
Figure 4. Unprocessed images of lunar horizon glow with observation times in Greenwich mean time. The Surveyor 1 image and one intermediate Surveyor 7 image are not shown. Zodiacal light is evident in the Surveyor 5 and 6 images but not in the Surveyor 7 images, perhaps because of the different camera iris settings. Photographs from National Space Science Data Center.

and Burke [1973] find $n_{pe} \sim n_{pe,0} \, z^{-1.2}$ in the magnetotail, leading to a more vertically distended photoelectron layer of more than 100 m above the surface. The solutions of *Nitter et al.* [1998] also show that the photoelectron layer profile does not change significantly with solar incidence angle for $i_s > 5°$.

[46] *De and Criswell* [1977] and *Criswell and De* [1977] estimate local electric fields due to shadows in the terminator region as high as 1000 V cm^{-1} on spatial scales on the order of 1 mm, though potential differences from one point to another were not greater than 100 V. These strong localized fields may play an important role in launching particles off the surface but would not be relevant for levitation of particles.

4. DUST CHARGING, LEVITATION, AND TRANSPORT

[47] Just as the Moon is subject to a number of charging currents, so are the individual dust particles on the lunar surface. Particles knocked off the lunar surface are subject to the same currents as the Moon as a whole, but these are modified because the dust particle may be in or moving through the plasma sheath near the lunar surface. Direct observations of dust above the lunar surface were made by the Surveyor spacecraft [*Criswell*, 1972, 1973, 1974; *Rennilson and Criswell*, 1974] and by Apollo 17 astronauts in the orbiting command module [*McCoy and Criswell*, 1974; *Zook and McCoy*, 1991]. Some of these observations have led to the development of a theory of electrostatic dust

levitation [*Singer and Walker*, 1962; *Walbridge*, 1973; *Pelizzari and Criswell*, 1978a, 1978b; *De and Criswell*, 1977; *Criswell and De*, 1977; *Nitter and Havnes*, 1992; *Nitter et al.*, 1994; *Doe et al.*, 1994; *Nitter et al.*, 1998; *Sickafoose et al.*, 2002]. The star-tracker camera on the Clementine spacecraft also imaged a glow along the lunar horizon that may be due to electrostatically transported lunar dust [*Zook et al.*, 1995]. High-altitude dust particles observed by the astronauts and possibly Clementine are too high for levitation to be the mechanism; these particles may be electrostatically accelerated away from the surface to high altitudes [*Stubbs et al.*, 2006] with some possibly escaping the Moon's gravity. In this section we review the evidence for charged dust above the lunar surface and describe experiments and modeling of charging and levitation of dust particles.

4.1. Observations of Lunar Horizon Glow

[48] The first direct evidence for electrostatic processes acting on lunar dust was a set of images taken by the television cameras on Surveyor 5, 6, and 7 and possible detection by Surveyor 1 [*Criswell*, 1973; *Rennilson and Criswell*, 1974]. These images, taken of the western horizon shortly after sunset, show a distinct glow just above the lunar horizon (Figure 4). Dubbed horizon glow (HG), this light was interpreted to be forward scattered sunlight from a cloud of levitated dust particles <1 m above the surface near the terminator. The horizon glow has a horizontal extent of about 3° on each side of the direction to the Sun. Assuming that the observed signal is dominated by diffraction of sunlight, this horizontal extent corresponds to spheres of

radius 5–6 μm for observations at visible wavelengths [*van de Hulst*, 1957]. The observed intensity of the signal, its duration (up to 2.5 hours), and its vertical and horizontal extent rule out micrometeoroid ejecta, scattering off surface grains, and reflections involving glints off the spacecraft [*Rennilson and Criswell*, 1974].

[49] The physical dimensions of the HG cloud require a determination of the distance to the cloud. By analyzing the shape of the lower boundary of the Surveyor 7 HG cloud and matching it to the local topography from orbital photographs of the Surveyor 7 landing site, *Rennilson and Criswell* [1974] place the cloud at the visible horizon or approximately 150 m from the spacecraft. The vertical extent of the cloud is 1.9 mrad or about 30 cm at that distance. This is comparable to the expected Debye length or photoelectron layer scale height and suggested that the particles were levitating in the photoelectron sheath. The stable levitation height, however, is at much higher elevations than this characteristic sheath scale height. Its horizontal extent of ~100 mrad makes the observed cloud 14 m wide, though this dimension may be a result of the light-scattering properties of the cloud: It could be much larger with the parts of the cloud farther from the Sun line not scattering sufficient light into the cameras.

[50] For a spherical Moon the shadow line is much higher than 30 cm 2 hours after sunset at a distance of only 150 m from the Surveyor. Two hours after sunset on the equator of the Moon the Sun is $\theta = 2\pi(2 \text{ hours}/708.7 \text{ hours}) = 17.7$ mrad below the horizon. The minimum height an object must be above the surface of a spherical body after sunset for it to be both illuminated and visible is

$$H = R_M \left(\sec \frac{\theta}{2} - 1 \right), \qquad (13)$$

where R_M is the radius of the Moon. Two hours after sunset this gives a minimum height for illumination by the Sun of 68 m in apparent contradiction to the HG images and the distance to the cloud calculated by *Rennilson and Criswell* [1974]. However, this assumes a perfectly spherical Moon. The visibility of the HG cloud within a meter of the lunar surface after sunset can be explained by the presence of positive topography on the western horizon relative to the position of the Surveyor spacecraft acting as an occulting screen for the Sun. Although the Sun is below the local horizon as seen from the spacecraft, the top of the ridge on the western horizon is both illuminated and visible.

[51] The determination that the Surveyor 7 HG cloud was located at the relatively near horizon (150 m distant) was based on analysis of morphology of the lower edge of the cloud and tying that morphology to craters observed in orbital photographs. The observations do not preclude the dust being more distant and correspondingly higher in altitude. The HG particles may be stably levitated at higher altitudes (section 4.4), or these particles may simply be on ballistic or electrostatically modified ballistic trajectories, and the top of the cloud is observed over the horizon. Strong localized surface electric fields at the terminator region could be responsible for the initial launching and acceleration of the particles. This is qualitatively consistent with other observations described in section 4.2.

[52] If the particles responsible for the HG are levitated, then there would be a gap between the bulk of the dust particles and the lunar surface. Analysis of the Surveyor images shows a gap in some of the images, which has been interpreted as the effective thickness of the photoelectron layer or plasma sheath and the levitation height of charged dust particles. The viewing geometry illustrated in Figure 4 demonstrates that it is not possible to see whether or not a dust cloud extends to the surface after sunset, because the visible surface is not illuminated and the illuminated surface is not visible. In the Surveyor 7 images, there is no gap between the HG and the lunar horizon, while an apparent gap in a Surveyor 6 image [*Rennilson and Criswell*, 1974, Figure 3b] may be due to overexposure and the camera's point spread function [*Rennilson and Criswell*, 1974]. The absence of a gap does not preclude the dust being in a stably levitating layer because the images may only show the top of that layer above the horizon while the gap and the source region are obscured beyond the horizon.

[53] Our analysis of the Surveyor images does show a bright band offset below the HG in some images. Two Surveyor HG images are shown in Figure 5. The images have been contrast enhanced to highlight any separation between the HG and the lunar surface. The Surveyor 6 image shows no apparent gap between the glow and the surface, consistent with a cloud of particles launched from the lunar surface but not necessarily levitating and at a distance therefore beyond the observable lunar horizon. The Surveyor 5 image of horizon glow similarly shows no break between the dust cloud brightness and the lunar horizon.

[54] The Surveyor 7 image, on the other hand, shows a bright area on the lunar surface, or surface shine, beneath the HG cloud, separated by a gap of comparable vertical extent to that of the cloud. If the upper extent of the surface shine is at the horizon, then this would indicate a gap beneath the HG cloud that could be explained either by a physical gap or by shadowing of a cloud connected to the surface. The illumination geometry argues against the surface shine coming from direct sunlight, and the horizontally restricted nature of the surface shine suggests an alternative interpretation: Some of the forward scattered light from the HG cloud is striking the lunar surface between the cloud and the spacecraft, producing a dimly illuminated area on the surface between the spacecraft and the horizon. The observed surface shine is strongly correlated with the brightest parts of the HG cloud, supporting this interpretation.

[55] Another indication of scattered light from dust above the lunar surface is the relatively high brightness recorded by the astrophotometer on the Lunokhod-2 rover [*Severny et al.*, 1975]. One measurement was made when the limb of the Sun was 17 mrad below the horizon, and the reading was roughly twice the value expected based on known light sources and the instrument response. The astrophotometer was directed toward the zenith, so illuminated dust would

Figure 5. Contrast enhanced and low-pass-filtered images of lunar horizon glow from (top) Surveyor 6 and (bottom) Surveyor 7. The apparent gap between the horizon glow and the lunar surface noted by *Rennilson and Criswell* [1974] can also be explained by forward scattering of light from the cloud itself to illuminate part of the lunar surface between the horizon and the spacecraft. Photographs from National Space Science Data Center.

have been more than 260 m above the surface to be a contributor to this source. The Lunokhod-2 dusk observation also would have been at about 90° phase angle for dust above the rover; the phase function for the small dust particles that could be electrostatically launched has a relatively low value in this geometry compared to the forward scattering geometry of the Surveyor observations. Other daytime measurements were also higher than expected, however, and there are no other observations indicating dust launched to high altitudes when the Sun is well above the horizon (see also section 4.2).

4.2. Observations by the Lunar Ejecta and Meteorites Experiment

[56] The Lunar Ejecta and Meteorites (LEAM) Experiment was deployed by the Apollo 17 astronauts as part of the Apollo Lunar Surface Experimental Package on 11 December 1972 (Figure 6). It started measurements after the return of the landing module and continued to make observations for about 3 years. The science objectives of LEAM were (1) to investigate the interplanetary dust flux (primary particles) bombarding the lunar surface; (2) to investigate the properties of the lunar ejecta (secondary) particles; (3) to follow the temporal variability of these fluxes along the lunar orbit; and (4) to observe interstellar particles. The design and the expected performance of the LEAM experiment are similar to those for the dust experiment onboard the Pioneer 8 and 9 spacecraft that were launched into heliocentric orbits in 1967 and 1968, respectively [*Berg and Richardson*, 1969; *Berg et al.*, 1973].

[57] The LEAM instrument consisted of three sensor systems. The east sensor was pointed 25° north of east, so

that once per lunation its field of view swept into the direction of the interstellar dust flow. The west sensor was pointing in the opposite direction as a control for the east sensor, while the up sensor was parallel to the lunar surface

Figure 6. Apollo 17 Lunar Surface Experiments Package. The box in the foreground is the Lunar Ejecta And Meteorites (LEAM) Experiment. NASA photograph AS17-134-20500, National Space Science Data Center.
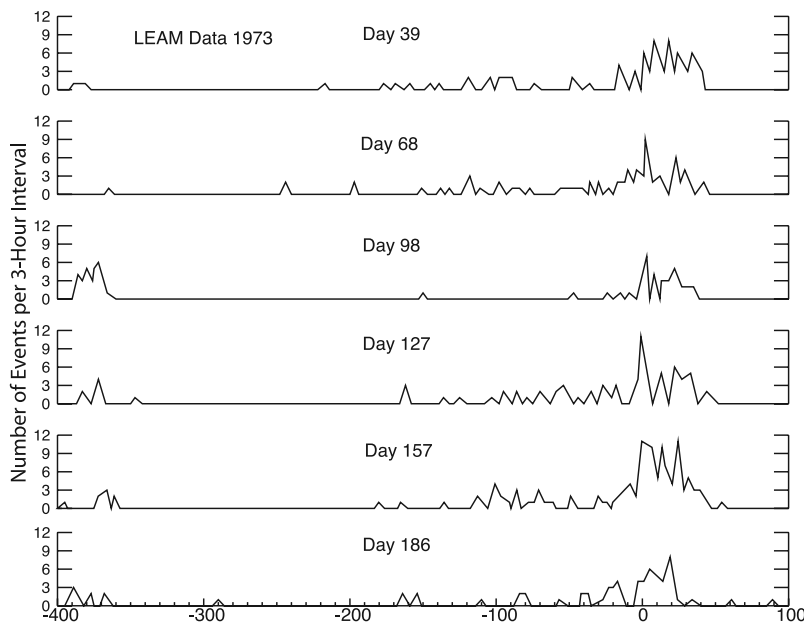
Figure 7. Number of impact events per 3-hour interval as a function of time [after *Berg et al.*, 1976].

and viewing particles coming from above. Each of these systems was composed of two sets (front and a back) of 4×4 basic sensor elements to determine the impacting particle's mass m and velocity vector $\mathbf{v}$. The sensors used a combination of thin plastic films and grids to measure the current from the plasma cloud generated as the dust particles penetrated the film, a signal pulse with amplitude proportional to $m\mathbf{v}^{2.6}$. The two groups of sensors in a system were placed 5 cm apart, and a time-of-flight system was used to determine the speed of an impacting dust particle. Each of the 16 front sensors were enabled to provide a start signal, and each of the 16 back sensors were designed to provide a stop signal for a total of 256 different combinations enabling the determination of the velocity vector of the penetrating dust particles. In addition, the back film was attached to a microphone with an acoustic signal proportional to the momentum of the grain.

[58] The only exception for this redundant arrangement was the west sensor, which lacked a front film. This sensor was designed to identify low-speed ejecta impacts that were expected not to penetrate the front film. Hence the west sensor could not measure particle speed. Extensive laboratory calibrations were performed on these sensors using a 2-MeV electrostatic accelerator with particle masses in the range of $10^{-13} < m < 10^{-9}$ g and velocities in the range of $1 < v < 25$ km s^{-1}. The pulse height amplitudes (PHA) from the film grid sensors were sorted in the range from 0 to 7, and in the preflight calibration the front film rarely registered a PHA greater than 3. Most preflight calibration dust impacts gave rise to signals from both films, indicating that the particles had penetrated the front film and passed on to the rear film.

[59] Once LEAM started to operate, it became clear that its observations contradicted expectations. On the basis of previous measurements in interplanetary space by Pioneer 8 and 9, for example, the expected impact rate of interplanetary dust

particles was a few impact detections per day. Instead, LEAM registered up to hundreds of impacts per day.

[60] Most puzzling was the fact that these events registered in the front film only but with the maximum possible PHA level of 7. Additionally, the LEAM operating temperature exceeded its predicted maximum value of 146° at lunar noon, indicating possible thermal problems that were initially believed to be responsible for generating noise in the electronics and possibly responsible for the elevated measured impact rates. This was supported by the correlation of the elevated impact rates with the passage of the terminator, both at sunrise and at sunset.

[61] As data accumulated, a systematic behavior was recognized. The terminator event rate started to increase up to 60 hours before the sunrise at the site and persisted for a period of approximately 30–60 hours. In this period the rates were up to 100 times higher than the normal background rates [*Berg et al.*, 1976]. The rates dropped 2 orders of magnitude during local noon. Interestingly, no increased rates were observed during lunar eclipses.

[62] Figure 7 shows the number of impact events per 3-hour period recorded by the east sensor for each of six lunations in 1973 [*Berg et al.*, 1976]. The traces start before sunset when LEAM was turned on and continue past sunrise when the instrument was turned off because of elevated temperatures. The up and west sensors exhibited similar behavior, though with a smaller amplitude. Figure 8 shows the number of dust impacts onto LEAM per 3-hour period, integrated over 22 lunar days.

[63] A new picture emerged to replace the high-temperature electronics explanation: LEAM was registering slow moving, highly charged lunar dust particles. There were two subsequent studies done to verify this point: a theoretical work to model the response of the electronics [*Perkins*, 1976] and an experimental study of the LEAM flight spare model [*Bailey and Frantsvog*, 1977]. The
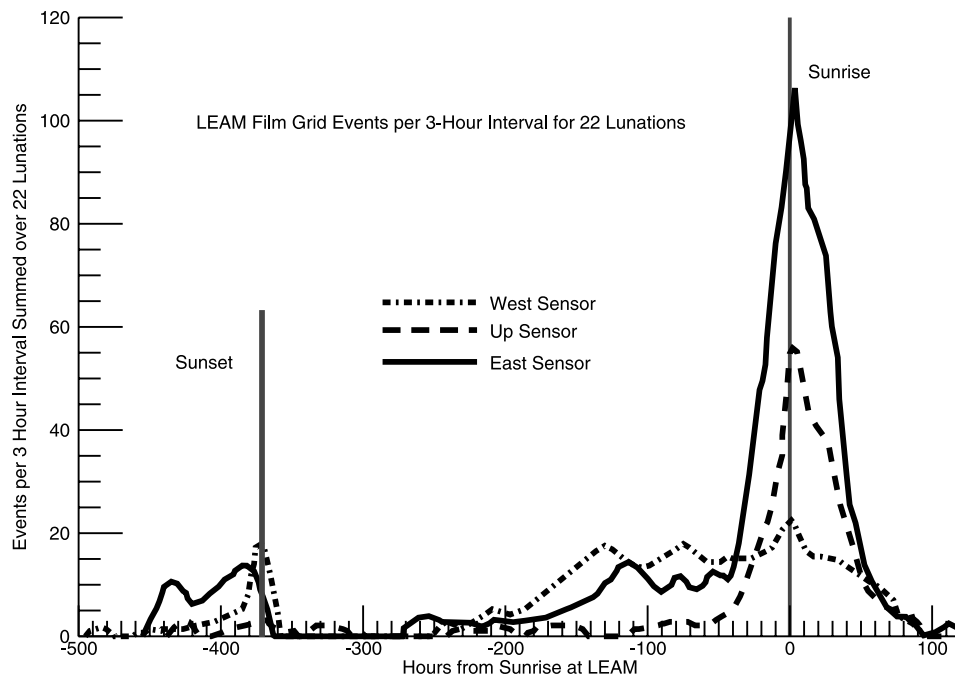
Figure 8. Number of impact events per 3-hour intervals integrated over 22 lunations [after *Berg et al.*, 1976]. The large increases at terminator crossings persist for several hours before and after sunrise and before the smaller increase at sunset, suggesting particles may be launched on long trajectories from the terminator.

results of the sensor modeling and circuit analysis showed that charged particles moving at velocities <1 km s^{-1} do produce large PHA responses via induced voltages on the entry grids, as opposed to signals from impact-generated plasmas. This explains why the rear films remained silent even though the front sensor was thought to be hit by an energetic dust grain. The experimental study had a similar conclusion: Extremely slow moving particles ($v < 100$ m s^{-1}) generate a LEAM response up to and including the maximum PHA of 7 if the particles carry a positive charge $Q > 10^{-12}$ C. Both of these studies suggest that the LEAM events are consistent with the sunrise/sunset–triggered levitation and transport of slow moving, highly charged lunar dust particles.

[64] The entire LEAM data set is shown in Figure 9 for all three sensor surfaces. While the daily average PHA remained relatively constant for the east and west sensors, it exhibited a rapid decline for the up sensor after 20 months, perhaps indicating dust accumulation on the topside of LEAM (O. Berg, personal communications, 2005).

4.3. Laboratory Measurements and Models of Dust Charging

4.3.1. Triboelectric Charging

[65] Even in the absence of charging currents described in section 3.1, grains in the lunar regolith will become charged because of the difference in contact potentials of grains and frictional transfer of charge between grains in contact. This triboelectric dust charging received little attention in the early literature on the lunar surface, perhaps because of a lack of a database on triboelectric charging of materials and the absence of accepted formulas for calculating the charge.
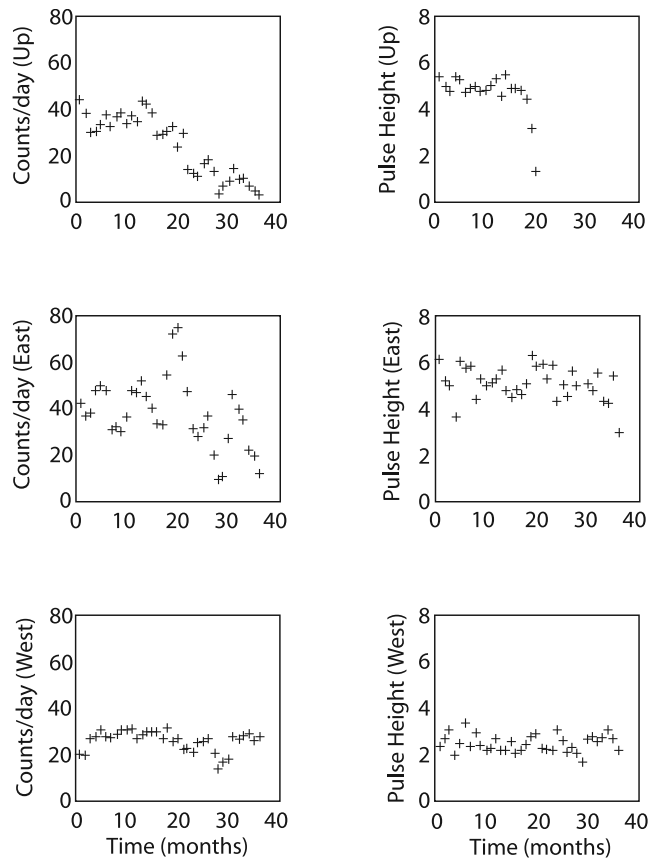

Figure 9. Monthly impact rates and average pulse heights for the entire LEAM period of observations (O. Berg, personal communication, 2005).
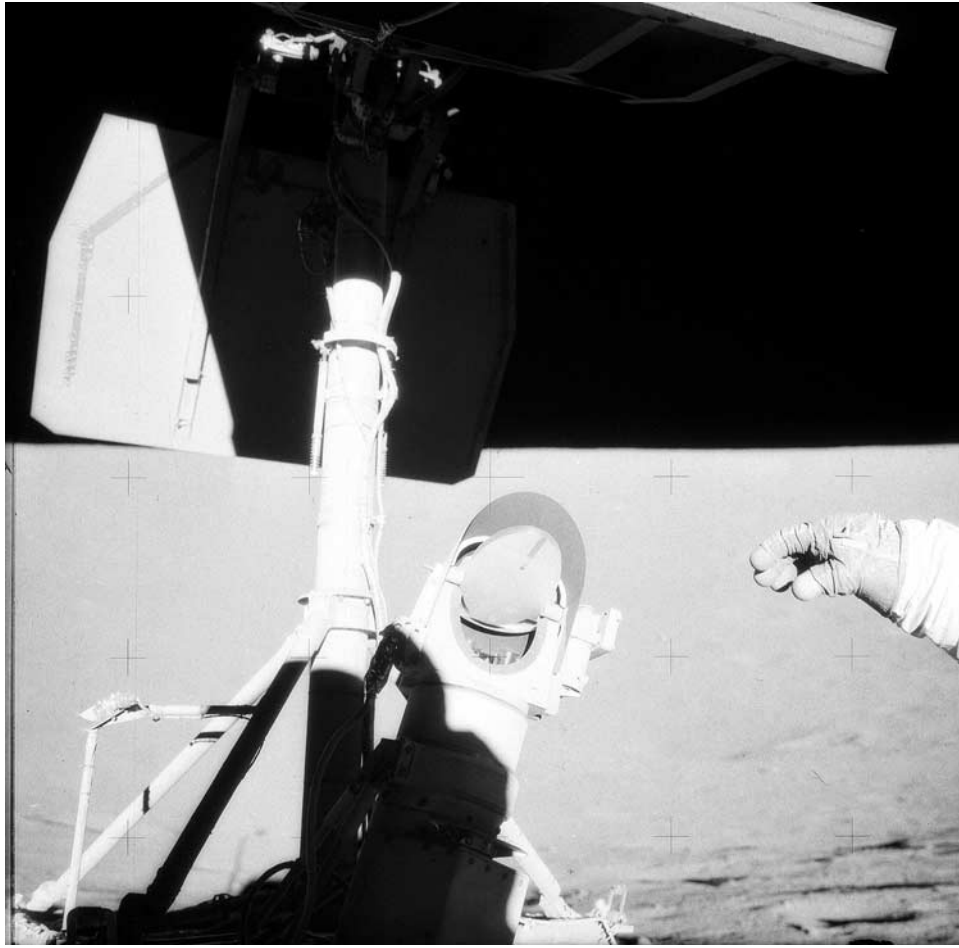
Figure 10. Apollo 12 astronaut Charles "Pete" Conrad Jr. gestures near the Surveyor 3 spacecraft on the lunar surface on 21 November 1969. The Surveyor 3 television mirror shows a finger mark made by Conrad in a layer of dust on the mirror. Surveyor 3 landed on the Moon on 20 April 1967, and dust was likely deposited on the mirror both during the landing of the Surveyor and also during the landing of the Apollo 12 Lunar Module some 155 m away. NASA photograph AS12-48-7132, Apollo 12 Principal Investigator Richard J. Allenby Jr., National Space Science Data Center.

Triboelectric charging in the laboratory often depends on the way in which materials have been prepared and stored, and this indicates a dependence on surface roughness, humidity, adsorbed gases, and other factors related to the history of the grain.

[66] *Sternovsky et al.* [2001] examined conducting and nonconducting materials that had been stored in vacuum, including lunar and Martian regolith simulants [*Sternovsky et al.*, 2002]. Dust particles were placed on a surface that was agitated so that particles fell individually through a small hole into a Faraday cup where the charge was measured. Grains with radii ≥ 25 μm were used in order to have a charge sufficiently large for measurement. The grains were placed sparsely on the surface so that the charging was because of contact with the surface rather than between grains. It was assumed that the charge while resting on the surface was not altered by passage through the hole. This assumption is supported by agreement between the data and the theory in cases that have a theoretical model (see sections 4.3.2 and 4.3.3). This experimental arrangement mimics dust on the surface of a spacecraft or instrument on the lunar surface (Figure 10).

[67] These experiments showed that in the absence of applied electric fields or UV illumination the charge on conducting grains resting on conducting surfaces was given approximately by $Q = CV$, where C is the capacitance between the grain and the conducting surface and V is the charging potential determined by the difference between the work function of the grain and of the surface. The capacitance is given approximately by

$$C = 4\pi\varepsilon_0 r_d \left[0.577 - \frac{1}{2} \ln(z_0/r_d) \right], \qquad (14)$$

where r_d is the grain radius. The parameter z_0 is the separation of the grain from the surface, which is dependent on the roughness of the materials. The difference in the tabulated work functions determines the charging potential V only in the case of unoxidized metals. For metals with oxide layers the effective work function is near to that typical of metallic oxides: $W \approx 5.5$ eV. For the
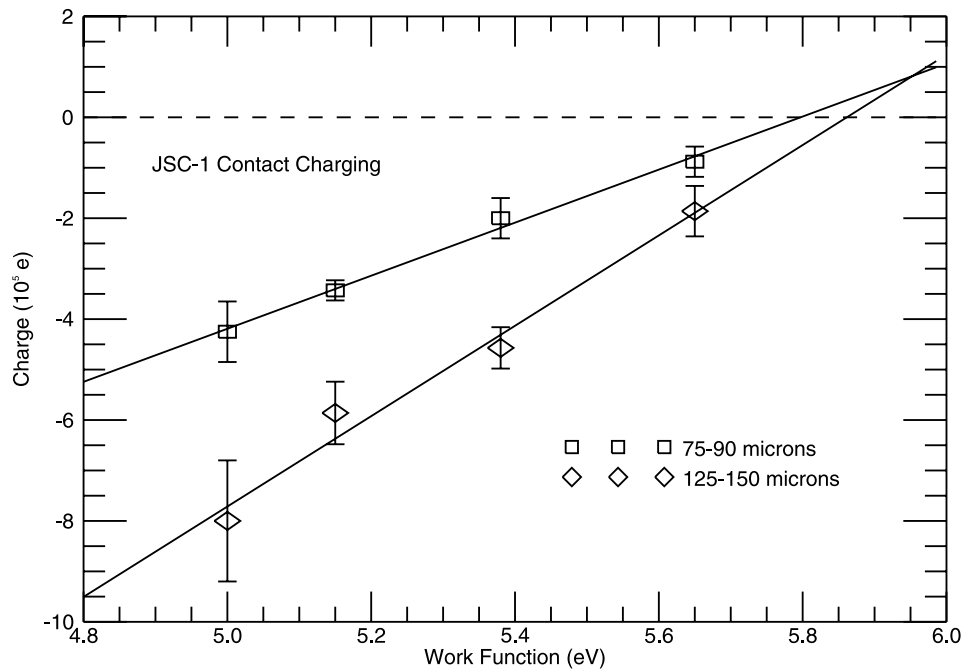
Figure 11. Charging of the lunar dust simulant JSC-1 from the metals Co, Ni, Au, and Pt. The horizontal scale is the work function of the metal surface. The JSC-1 samples were sieved to two different size ranges. The points represent the average dust charge from six individual measurements with the standard deviations indicated by the error bars. The solid lines are linear fits to the data and indicate a contact charging work function of JSC-1 of about 5.8 eV. From *Sternovsky et al.* [2002].

nonconductors alumina and silica on metallic surfaces the effective work functions were 5.25 eV and 5.5 eV, respectively. The deduced work function for the lunar simulant JSC-1 is $W_{JSC-1} = 5.8$ eV (Figure 11). Measurements were made of the work function for two different size ranges of JSC-1 particles with no significant difference between the two [*Sternovsky et al.*, 2002].

[68] Conducting grains on conducting surfaces were found to have an additional induced charge when an electric field was imposed at the surface. The additional charge is approximately the value expected from Gauss' law, taking into consideration the enhancement of the electric field at the site of the particle:

$$Q_{induced} \approx 6.6\varepsilon_0 E\pi r_d^2, \quad (15)$$

where E is the electric field.

[69] The triboelectric charge on grains in contact with other grains was determined by placing relatively thick layers of dust in the dropper so that contact with the metallic surface of the dropper was minimized [*Sickafoose et al.*, 2001]. In this case the grain charge had a broad distribution roughly centered on zero charge (Figure 12). There were approximately an equal number of positively and negatively charged grains, and the magnitude of the charge on 100-μm grains was $\sim 10^5$ electrons, corresponding to charging potentials in the range of +2 V to −2 V.

4.3.2. Photoelectric Charging

[70] Several laboratory experiments have been performed to observe photoelectric charging and transport of dust. The

brightest laboratory UV sources are 1 kW Xe arc lamps with quartz envelopes that pass wavelengths longer than $\lambda = 200$ nm (photon energies $E_\gamma < 6$ eV). Photoemission created by the solar spectrum is dominated by Lyman alpha emission ($\lambda = 121.6$ nm and $E_\gamma = 10.2$ eV). Lamps with windows that transmit to 100 nm are limited to about 30 W, which results in charging times that are too short for many types of experiments. This makes photoelectron production from lunar regolith simulants difficult given the relatively high work function of 5.8 eV (section 4.3.1). A typical photocurrent density from artificial satellite materials in space is $2-8$ nA cm^{-2}, and the photoelectron temperature is ~ 2 eV [*Willis et al.*, 1973]. Photocurrents of ~ 20 μA can be obtained with the Xe arc lamp from surfaces with low work functions and high photoelectron yields such as zirconium (Zr) metal foil ($W = 4.05$ eV). This results in a photoelectron energy distribution that is truncated at about 2 eV (E_γ - W).

[71] Just as the dayside of the Moon acquires a positive charge because of photoelectron emission, isolated individual dust particles exposed to UV radiation charge positively until the charging potential is sufficient to return emitted electrons. The charging potential on an isolated grain in UV light, with no other currents, is then given by

$$\Phi_d = (E_\gamma - W)/e, \quad (16)$$

where e is the elementary charge and the charge on the grain is related to the potential of the dust particle relative to the surrounding plasma, Φ_d, by

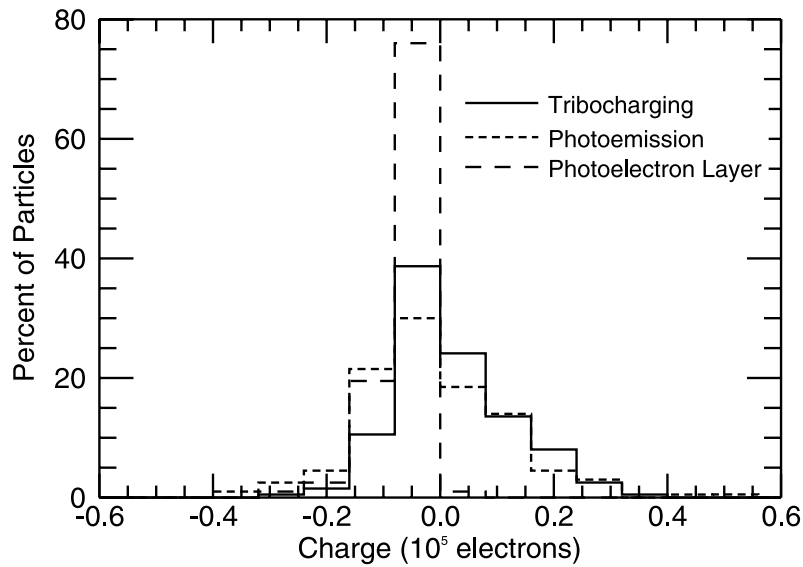$$Q = C\Phi_d = 4\pi\varepsilon_0 r_d \Phi_d, \quad (17)$$

Figure 12. Distribution of charges on grains of JSC-1 lunar regolith simulant under three different charging conditions. The solid line shows the distribution of charges in the absence of any plasma or UV radiation when the particles were dropped from a pile one at a time. The charges in this case are a result of triboelectric charging from grain-grain contacts. The dotted line is for the case where the particles were illuminated by UV radiation. There is a slight shift of the charge distribution to negative charges, although photoemission would tend to make the charges less negative. This indicates that in this case triboelectric charging is the dominant charge process. The dashed line is for particles falling through a photoelectron layer. In this case, almost all particles charged slightly negative through collection of photoelectrons from the layer. From *Sickafoose et al.* [2001].

where the capacitance for an isolated sphere, $C = 4\pi\varepsilon_0 r$, differs from that given in equation (14) for a particle on a surface. This expression for grain charge has been verified by dropping conducting grains with different work functions through UV radiation and measuring the resulting charge [*Sickafoose et al.*, 2000, 2001].

[72] A different charge results when a grain is exposed to UV radiation but is within the photoelectron layer of a larger object (such as the Moon). Here the competing current of photoelectrons from the photoelectron layer to the grain can overcome the current because of photoelectrons leaving the grain, and the grain can acquire a negative charge. This change in grain charge from positive (outside the photoelectron layer) to negative (inside the photoelectron layer) depends on the density of photoelectrons in the layer (equation (11)). This change in sign of the grain charge with distance above a photoemitting surface was verified experimentally by placing grains at different distances from a vertical Zr plate exposed to UV radiation [*Sickafoose et al.*, 2001]. The time the grains spent in the photoelectron layer produced by the plate was several orders of magnitude longer than the grain charging time, so the grains reached an equilibrium charge. Additional experiments illustrated the change in the distribution of charges acquired by grains in the presence and absence of UV radiation and a photoelectron layer (Figure 12). Within the photoelectron layer, grains have a negative charge because of the collection of photoelectrons from the surface. Because the electric field in the photoelectron layer is directed upward, grains must be above the photoelectron layer to have a positive charge

from their own photoemission in order to be levitated or accelerated away from the surface.

4.3.3. Charging in a Plasma

[73] Plasma charging and photoelectric emission are the competing charging processes for dust particles that are above the photoelectron layer, where the thickness of the layer is given by the effective Debye length for the layer (equation (12)). Solar wind electrons have approximately a Maxwellian distribution, and the protons can be described as a monoenergetic beam. These distributions can be reproduced near a negatively biased surface in a laboratory plasma device. Near the surface, ions are accelerated and have a nearly monoenergetic distribution with an energy that depends on the distance from the surface and the potential of the surface. The electrons remain Maxwellian. The charging current from thermal electrons to a particle of radius r with a negative surface potential, Φ_d, is given by

$$I_e = -\pi r^2 n e \sqrt{\frac{8E_e}{\pi m_e}} \exp\left[\frac{e\Phi_d}{E_e}\right], \qquad (18)$$

and the current from ions is

$$I_i = \pi r^2 n e \sqrt{\frac{2E_i}{m_i}} \left[1 - \frac{e\Phi_d}{E_i}\right], \qquad (19)$$

where n is the ion and electron density, $E_e = kT_e$ is the electron temperature in eV, k is the Boltzmann constant, $E_i = 1/2 m_i v_i^2$ is the ion kinetic energy, and m_i and m_e are their masses. The floating potential of the grain Φ_d is found

by setting the net current to zero, and the grain charge is then determined from equation (17).

[74] The charging of grains is a fundamental part of the dynamics of dust in the lunar plasma environment. In the natural lunar surface environment, plasma charging, photoemission, and contact charging determine the charges on individual grains. Human or spacecraft activity can induce triboelectric charging as well as higher contact charging if dust particles are deposited on equipment with lower work function materials. Experiments support the picture of relatively broad distributions of charges on particles in the regolith. Once particles are knocked off the surface, either from impacts, electrostatic levitation, or human activity, their charges readjust to the ambient plasma conditions. There is currently no theory for the charge distribution of grains in a regolith, but recent experiments have been performed that show that the charge of the particles is tied to the overall surface charge density, with some spread due to contact and tribocharging [*Wang et al.*, 2007]. On larger grains (tens of microns) the charge appears to be in stable patches on the surface of the particle. Dust deposited onto equipment on the lunar surface can therefore be a charge carrier. The distribution of charges on grains in the regolith is important in determining the ability of particles to initially electrostatically levitate. However, the particles observed and predicted to move in the lunar plasma sheath are smaller than those that have been experimentally studied for regolith charging. Further experiments, as well as future measurements of the plasma environment and dust mobility at the lunar surface, are needed to understand the charge state of regolith particles on the Moon and other airless bodies in the solar system. In section 4.4 we review the status of charged dust levitation and transport with our current understanding of dust charging and of photoelectron and plasma sheath electric fields.

4.4. Laboratory Measurements and Models of Dust Levitation and Transport

[75] Laboratory studies of charged dust levitation have focused on levitation in a plasma sheath rather than a photoelectron sheath because it is easier to generate the electric fields necessary for levitation in a plasma. In experiments [*Arnas et al.*, 2001; *Sickafoose et al.*, 2002], grains are observed to levitate above a negatively biased surface because of the negative grain charge and downward pointing electric field. The grain charge is calculated in these experiments by determining the necessary electric force to counter gravity at the observed position with the sheath. The electric field is measured by scanning probes near the biased surface (Figure 3), and from these measurements the charge is determined. The experiments show good agreement between the charge calculated from the model equations (equations (18) and (19) give Φ_d by setting the net current to zero) and the charge deduced from force balance,

$$\frac{4}{3}\pi r_d^3 \rho_d g = -4\pi\varepsilon_0 r_d \Phi_d(z)\frac{\partial\Phi(z)}{\partial z}, \qquad (20)$$

where ρ_d is the density of the dust particle and g is the acceleration due to gravity. In equation (17) all parameters are known, and the gradient in the sheath potential (the electric field) is determined from plasma measurements (Figure 3), so the particle potential Φ_d can be computed for comparison to the value obtained from looking at the currents to the particle.

[76] Roughly speaking, the electric field at the base of the photoelectron layer is given by the surface potential divided by the shielding distance or effective Debye length of the photoelectron layer. There are two locations in the photoelectron layer or plasma sheath at which the electric force can balance the gravitational force. The lower of these potential levitation heights is roughly one Debye length above the surface, but particles at this height are unstable [*Nitter et al.*, 1998; *Robertson et al.*, 2003]. Just below the lower equilibrium height, particles are accelerated down to the surface, while those above it will settle into the upper equilibrium height.

[77] If we know the functional form of the electric field with height above the surface, then the upper (stable) equilibrium height can be evaluated analytically by assuming that particles at that height are far enough above the sheath so that the charge on the grain is dominated by the solar wind [*Colwell et al.*, 2005]. The electric field strength as a function of height above the surface in a photoelectron sheath whose density is described by equation (11) for a Maxwellian photoelectron velocity distribution is given by [*Grard and Tunaley*, 1971]

$$E(z) = E_0\left[1 + \frac{z}{\sqrt{2}\lambda_D}\right]^{-1}. \qquad (21)$$

[78] This vertical profile has also been produced using particle-in-cell numerical simulations of an emitting plate (J. E. Colwell et al., Lunar dust levitation, submitted to *Journal of Aerospace Engineering*, 2006, hereinafter referred to as Colwell et al., submitted manuscript, 2006). Substituting this expression for the electric field into equation (17) and assuming particles have a potential in volts, $\Phi_{d,sw}$, determined solely by the solar wind, we obtain the following expression for the upper equilibrium height:

$$z_{eq} = \sqrt{2}\lambda_D\left[\frac{3\varepsilon_0 E_0 \Phi_{d,sw}}{\rho_d g r_d^2} - 1\right], \qquad (22)$$

where r_d is the particle radius, ρ_d is the density, and g is the gravitational acceleration. The levitation height increases rapidly for particles smaller than the largest particle that can be levitated $r_{d,max}$. Particles one tenth the size of r_{dmax}, for example, have a levitation height of roughly 100 m for the value of $\lambda_D = 66$ cm calculated for a photoelectron layer in section 3.3. For dust particles on the Moon with $\rho_d = 3$ g cm^{-3} the condition for levitation is

$$r_{d,max} = 0.074\sqrt{E_0\Phi_{d,sw}}\mu\text{m}, \qquad (23)$$

where E_0 is in V m^{-1} and $\Phi_{d,sw}$ is measured in volts. For a surface electric field of 10 V m^{-1} and a typical dust charge
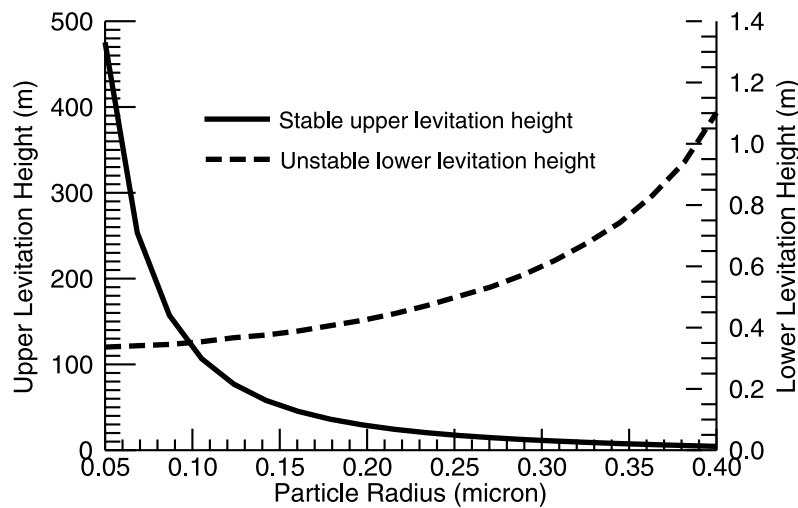
Figure 13. The upper (stable) levitation height and lower (unstable) levitation height for submicron grains in the lunar photoelectron layer using the model of *Colwell et al.* [2005] with a photoemission current of 2.8×10^{10} electrons cm^{-2} s^{-1}.

in the solar wind the largest particle that can be stably levitated has $r_d \sim 0.5$ μm. Sample calculated levitation heights as a function of particle size are shown in Figure 13 where the photoemission current from the lunar regolith was increased by a factor of 10 over the value given before equation (10) in order to produce a sufficient surface electric field to support particles of this size.

[79] This general picture of levitation in a plasma sheath has been verified experimentally [*Arnas et al.*, 2001; *Sickafoose et al.*, 2002]. If the sheath is not uniform or if the particles leave the surface with any horizontal velocity, then there can be transport of dust across the surface. For example, particles launched in a photoelectron layer may precipitate into shadowed regions where the electric field vanishes. The scale of the shadowed region necessary to effect such precipitation would likely need to be comparable to the levitation height. On a smaller scale, particles may move on ballistic trajectories from areas of one surface potential to another where electrostatic launching from the surface is less likely.

[80] This theory assumes that the charge carried by the dust particles does not affect the plasma. If a large amount of charged dust is levitated or even moving through the sheath, that charge will affect the potential profile of the sheath. The charged grains will also affect each other through Coulomb interactions, leading to a redistribution of dust. Experiments show horizontal transport of dust when an initial spot of dust is placed on a graphite plate. Horizontal electric fields are generated at the boundary of the dust spot because of the different charging properties of the dust and the plate. The dust redistributes itself to smooth out this potential difference, which, in turn, reduces the horizontal electric field strength and stops the horizontal transport process (Colwell et al., submitted manuscript, 2006). On the Moon such redistribution may not occur since the surface has essentially uniform electrical properties and the dust coverage is essentially global. Spacecraft components can introduce small-scale heterogeneities, how-

ever, which could give rise to localized electric fields at the surface that will precipitate charged dust transport.

5. SUMMARY AND CONCLUSIONS

[81] The geotechnical properties for engineering with lunar regolith have been determined through both in situ testing of and ground experimentation with both lunar regolith and manufactured simulants. The interlocking nature of lunar regolith due to the presence of angular particles and agglutinates results in increased strength, in both friction angle and cohesion intercept, over typical terrestrial soils. The near-surface regolith is probably characterized well enough to guide designing such things as berms and shallow excavations and to begin development of equipment. However, there is a lack of solid information on the density and grain size distribution, including larger inclusions, at depths of more than a meter or two. It is also thought that the surface material is fairly uniform from a geotechnical perspective, with the exception of recent craters that can expose coarser material. The largest challenge for physical manipulation (excavations and processing) and mobility is in design of equipment and methodology of use. Excavation of lunar regolith, particularly in the dense region found below about 0.3 m in depth, is a challenge that must be addressed. Above that the regolith is more penetrable but will pose challenges for mobility, particularly in regions of very low relative density such as near fresh crater rims and with more massive transport vehicles. Engineering effectively will require novel solutions to deal with the unique environment as well as the unique material.

[82] The discussion of levitation in section 4 is for a full daytime photoelectron layer. At some times in the lunar day, perhaps near the terminator and also in the Earth's magnetotail, the surface potential and electric fields may be much larger, allowing larger particles to be launched off the surface (section 3.1). There are a number of lines of observational evidence for dust moving over the lunar

surface from electrostatic processes (sections 4.1–4.2). These observations show a strong link between dust activity and the terminator crossing when the surface potential and electric fields are changing and can be locally higher than typical daytime or nighttime values. These observations are consistent with a picture of the finest fraction of the lunar regolith being electrostatically launched off the surface of the Moon and following modified ballistic trajectories. These dust particles may be reaching heights of anywhere from a few to hundreds of meters and are likely ~ 1 μm in size. At high altitudes above the surface the particles may be submicron, while larger grains may be restricted to the first few meters above the surface because of their smaller charge to mass ratio.

[83] Stable levitation of charged dust particles is not needed to explain the observations of dust over the lunar surface. Surveyor observations of lunar horizon glow may be of dust particles on essentially ballistic trajectories, though levitation cannot be ruled out (section 4.1). Given the strong dependence of levitation height on particle size (equation (22)), any size distribution of levitated grains would produce a cloud with a large vertical extent, with the detailed vertical profile dependent on the exact size distribution.

[84] Future exploration activities on the lunar surface, both manned and unmanned, will take place in a complex and time-variable plasma environment on a surface with unusual engineering properties and micron-sized dust that can lift off the surface to large altitudes. New approaches to working with the dense, angular lunar regolith and mitigating dust contamination will be a necessary component of long-duration stays on the lunar surface. Apollo astronaut spacesuits became coated with regolith, and optical components were covered with visible dust layers. The landing of the Apollo 12 lunar module 183 m from the Surveyor 3 lander resulted in a ''sandblasting'' of the Surveyor spacecraft [*Vaniman et al.*, 1991b]. New in situ experiments are needed to explore the mechanical properties of the regolith at depths below the first few decimeters and to understand the relationship between charged dust mobility and the surface plasma environment. Langmuir probes can measure the electron and ion densities and temperatures, and deployable booms can measure the near-surface electric field over the course of several lunar days. In situ dust detectors including piezoelectric sensors, charged dust detectors, and optical experiments can be deployed on the lunar surface to measure dust transport simultaneously with the plasma measurements. A better understanding of the mechanical properties of lunar dust as well as its dynamical response to the changing lunar plasma environment will help in devising dust mitigation strategies for future lunar exploration.

REFERENCES

Arnas, C., M. Mikikian, and F. Doveil (1999), High negative charge of dust particles in a hot cathode discharge, *Phys. Rev. E*, *60*(6), 7420–7425.

Arnas, C., M. Mikikian, G. Bachet, and F. Doveil (2000), Sheath modification in the presence of dust particles, *Phys. Plasmas*, *7*, 4418–4422.

Arnas, A., M. Mikikian, and F. Doveil (2001), Micro-sphere levitation in a sheath of a low pressure continuous discharge, *Phys. Scr. T*, *89*, 163–167.

Bailey, C. L., and D. J. Frantsvog (1977), Response of the LEAM detector to positively charged microparticles, report, NASA contract NAS5–23557, Concordia Coll., Moorhead, Minn.

Berg, O. E., and F. F. Richardson (1969), The Pioneer 8 cosmic dust experiment, *Rev. Sci. Instrum.*, *40*, 1333–1337.

Berg, O. E., F. F. Richardson, and H. Burton (1973), Lunar ejecta and meteorites experiment, in *Apollo 17 Preliminary Science Report*, NASA Spec. Publ., SP-330, 16-1–16-9. (Available at http://www.history.nasa.gov/alsj/main.html)

Berg, O. E., H. Wolf, and J. Rhee (1976), Lunar soil movement registered by the Apollo 17 cosmic dust experiment, in *Interplanetary Dust and Zodiacal Light*, edited by H. Elsasser and H. Fechtig, pp. 233–237, Springer, New York.

Bharuthram, R., M. A. Hellberg, P. K. Shukla, and F. Verheest (Eds.) (2002), *Dusty Plasmas in the New Millennium, Third International Conference on the Physics of Dusty Plasmas*, AIP Conf. Proc., *649*, 516 pp.

Bohm, D. (1949), *The Characteristics of Electrical Discharges in Magnetic Fields*, edited by A. Guthrie and R. K. Wakerling, McGraw-Hill, New York.

Cadenhead, D. A., M. G. Brown, D. K. Rice, and J. R. Stetter (1977), Some surface area and porosity characterizations of lunar soils, *Proc. Lunar Sci. Conf.*, *8th*, 1291–1303.

Carrier, W. D., III (2003), Particle size distribution of lunar soil, *J. Geotech. Geoenviron. Eng.*, *129*(10), 956–959.

Carrier, W. D., L. G. Bromwell, and R. T. Martin (1972), Strength and compressibility of returned lunar soil, *Proc. Lunar Sci. Conf.*, *3rd*, 3223–3234.

Carrier, W. D., III, J. K. Mitchell, and A. Mahmood (1973), The nature of lunar soil, *J. Soil Mech. Found. Div. Am. Soc. Civ. Eng.*, *99*, 813–832.

Carrier, W. D., G. R. Olhoeft, and W. Mendell (1991), Physical properties of the lunar surface, in *The Lunar Sourcebook*, edited by G. Heiken, D. T. Vaniman, and B. M. French, pp. 475–594, Cambridge Univ. Press, New York.

Chambers, J. G., L. A. Taylor, A. Patchen, and D. S. McKay (1995), Quantitative mineralogical characterization of lunar high-Ti mare basalts and soils for oxygen production, *J. Geophys. Res.*, *100*, 14,391–14,401.

Colwell, J. E. (2003), Low velocity impacts into dust: Results from the COLLIDE-2 microgravity experiment, *Icarus*, *164*, 188–196, doi:10.1016/S0019-1035(03)00083-6.

Colwell, J. E., and M. Taylor (1999), Low-velocity microgravity impact experiments into simulated regolith, *Icarus*, *138*, 241–248.

Colwell, J. E., A. A. S. Gulbis, M. Horányi, and S. Robertson (2005), Dust transport in photoelectron layers and the formation of dust ponds on Eros, *Icarus*, *175*, 159–169.

Cremers, C. J., R. C. Birkebak, and J. P. Dawson (1970), Thermal conductivity of fines from Apollo 11, in *Proceedings of Apollo 11 Lunar Science Conference*, edited by A. A. Levinson, *Geochim. Cosmochim. Acta Suppl.*, 1, 2045–2050.

Criswell, D. R. (1972), Lunar dust motion, *Proc. Lunar Sci. Conf.*, 3rd, 2671–2680.

Criswell, D. R. (1973), Horizon-glow and the motion of lunar dust, in *Photon and Particle Interactions With Surfaces in Space*, edited by R. J. L. Grard, pp. 545–556, Springer, New York.

Criswell, D. R. (1974), Sunset intensification of lunar surface electric fields (abstract), in *Lunar Interactions*, edited by D. R. Criswell and J. R. Freeman, pp. 100–102, Lunar Sci. Inst., Houston, Tex.

Criswell, D. R., and B. R. De (1977), Intense localized charging in the lunar sunset terminator region: 2. Supercharging at the progression of sunset, *J. Geophys. Res.*, 82, 1005–1007.

De, B. R., and D. R. Criswell (1977), Intense localized photoelectric charging in the lunar sunset terminator region: 1. Development of potentials and fields, *J. Geophys. Res.*, 82, 999–1004.

Doe, S. J., O. Burns, D. Pettit, J. Blacic, and P. W. Keaton (1994), The levitation of lunar dust via electrostatic forces, in *Engineering, Construction, and Operations in Space*, pp. 907–915, Am. Soc. of Civ. Eng., Reston, Va.

Freeman, J. W., and M. Ibrahim (1975), Lunar electric fields, surface potential and associated plasma sheaths, *Moon*, 8, 103–114.

Freitag, D. R., A. J. Green, and K.-J. Melzer (1970), Performance evaluation of wheels for lunar vehicles (summary report), *Misc. Pap. M-70-4*, NASA, U. S. Army Eng. Waterways Exp. Sta., Vicksburg, Miss.

Goertz, C. K. (1989), Dusty plasmas in the solar system, *Rev. Geophys.*, 27, 271–292.

Görz, H., W. E. White, R. Roy, and G. G. Johnson (1971), Particle size and shape distributions of lunar fines by CESEMI, *Proc. Lunar Sci. Conf.*, 2nd, 2021–2025.

Görz, H., E. W. White, G. G. Johnson, and M. W. Pearson (1972), CESEMI studies of Apollo 14 and 15 fines, *Proc. Lunar Sci. Conf.*, 3rd, 3195–3200.

Grard, R. J. L., (Ed.) (1973), *Photon and Particle Interactions With Surfaces in Space*, *Proceedings of the* 6th *ESLAB Symposium*, *Held at Noordwijk*, *The Netherlands*, 26–29 September 1972, Springer, New York.

Grard, R. J. L., and J. K. E. Tunaley (1971), Photoelectron sheath near a planetary probe in interplanetary space, *J. Geophys. Res.*, 76, 2498–2505.

Green, A. J., and K.-J. Melzer (1971), Performance of Boeing LRV wheels in a lunar soil stimulant: Effect of wheel design and soil, *Tech. Rep. M-71-10*, U. S. Army Eng. Waterways Exp. Sta., Vicksburg, Miss.

Grün, E., H. A. Zook, H. Fechtig, and R. H. Giese (1985), Collisional balance of the meteoritic complex, *Icarus*, 62, 244–272.

Halekas, J. S., D. L. Mitchell, R. P. Lin, L. L. Hood, M. H. Acuña, and A. B. Binder (2002), Evidence for negative charging of the lunar surface in shadow, *Geophys. Res. Lett.*, 29(10), 1435, doi:10.1029/2001GL014428.

Halekas, J. S., R. P. Lin, and D. L. Mitchell (2005), Large negative lunar surface potentials in sunlight and shadow, *Geophys. Res. Lett.*, 32, L09102, doi:10.1029/2005GL022627.

Hartmann, W. K. (1980), Dropping stones in magma oceans: Effects of early lunar cratering, in *Proceedings of the Conference on the Lunar Highlands Crust*, edited by J. J. Papike and R. B. Merrill, pp. 155–171, Elsevier, New York.

Hartmann, W. K. (1985), Impact experiments, 1, Ejecta velocity distributions and related results from regolith targets, *Icarus*, 63, 69–98.

Heywood, H. (1971), Particle size and shape distribution for lunar fines sample 12057,72, *Proc. Lunar Sci. Conf.*, 2nd, 1989–2001.

Holsapple, K. A. (1993), The scaling of impact processes in planetary sciences, *Annu. Rev. Earth Planet. Sci.*, 21, 333–373.

Horányi, M., B. Walch, S. Robertson, and D. Alexander (1998), Electrostatic charging properties of Apollo 17 lunar dust, *J. Geophys. Res.*, 103, 8575–8580.

Hörz, F., H. Gall, R. Huttner, and V. R. Oberbeck (1977), Shallow drilling in the "Bunte Breccia" impact deposits, Ries Crater, Germany, in *Impact and Explosion Cratering*, edited by D. J. Roddy, R. O. Pepin, and R. B. Merrill, pp. 425–558, Elsevier, New York.

Hörz, F., G. Grieve, G. Heiken, P. Spudis, and A. Binder (1991), Lunar surface processes, in *The Lunar Sourcebook*, edited by G. Heiken, D. T. Vaniman, and B. M. French, pp. 61–111, Cambridge Univ. Press, New York.

Houck, K. J. (1982), Petrologic variations in Apollo 16 surface soils, *Proc. Lunar Planet. Sci. Conf., 13th, Part I, J. Geophys. Res.*, 87, suppl., A197–A209.

Housen, K., R. Schmidt, and K. Holsapple (1983), Crater ejecta scaling laws: Fundamental forms based on dimensional analysis, *J. Geophys. Res.*, 88, 2485–2499.

Houston, W. N., J. K. Mitchell, and W. D. Carrier III (1974), Lunar soil density and porosity, *Proc. Lunar Sci. Conf.*, 5th, 2361–2364.

Jaffe, L. D. (1971), Bearing strength of lunar soil, *Moon*, 3, 337–345.

Jaffe, L. D. (1973), Shear strength of lunar soil from Oceanus Procellarum, *Moon*, 8, 58–72.

Jaky, J. (1944), The coefficient of Earth pressure at rest, *J. Soc. Hung. Arch. Eng.*, 7, 355–358.

Klosky, J. L., S. Sture, H. Y. Ko, and F. Barnes (1995), Augured foundations of lunar operations, in *Proceedings of the* 3rd *International Symposium on Mine Mechanization and Automation*, vol. 2, pp. 112–124, Colo. Sch. of Mines, Golden, Colo.

Klosky, J. L., S. Sture, H. Y. Ko, and F. Barnes (1996), Vibratory excavation and anchoring tools for the lunar surface, *Proc. Space V, Eng. Construct. Oper. Space*, 2, 903–909.

Klosky, J. L., S. Sture, H.-Y. Ko, and F. Barnes (2000), Geotechnical behavior of JSC-1 lunar regolith simulant, *J. Aerosp. Eng.*, 13(4), 680–688.

Ko, H.-Y., and S. Sture (1980), Data reduction and applications for analytical modeling: State-of-the-art, *Spec. Tech. Publ. STP 740*, pp. 329–386, Am. Soc. for Test. and Mater., West Conshohocken, Pa.

Lambe, T. W., and R. V. Whitman (1969), *Soil Mechanics*, John Wiley, Hoboken, N. J.

Le Mouélic, S., Y. Langevin, S. Erard, P. Pinet, S. Chevrel, and Y. Daydou (2000), Discrimination between maturity and composition of lunar soils from integrated Clementine UV-visible/near-infrared data: Application to the Aristarchus Plateau, *J. Geophys. Res.*, 105, 9445–9455.

Lieberman, M. A., and A. J. Lichtenberg (1994), *Principles of Plasma Discharge and Materials Processing*, John Wiley, Hoboken, N. J.

Manka, R. H. (1973), Plasma and potential at the lunar surface, in *Photon and Particle Interactions With Surfaces in Space*, edited by R. J. L. Grard, pp. 347–361, Springer, New York.

McCoy, J. E., and D. R. Criswell (1974), Evidence for a high latitude distribution of lunar dust, *Proc. Lunar Sci. Conf.*, 5th, 2991.

McKay, D. S., G. Heiken, A. Basu, G. Blanford, S. Simon, R. Reedy, B. M. French, and J. Papike (1991), The lunar regolith, in *The Lunar Sourcebook*, edited by G. Heiken, D. T. Vaniman, and B. M. French, pp. 285–356, Cambridge Univ. Press, New York.

McKay, D. S., J. L. Carter, W. W. Boles, C. C. Allen, and J. H. Allton (1994), JSC-1: A new lunar soil simulant, in *Engineering, Construction and Operations in Space IV*, pp. 857–866, Am. Soc. of Civ. Eng., Reston, Va.

Mitchell, J. K., W. N. Houston, R. F. Scott, N. C. Costes, W. D. Carrier III, and L. G. Bromwell (1972a), Mechanical properties of lunar soil: Density, porosity, cohesion, and angle of friction, *Proc. Lunar Sci. Conf.*, 3rd, 3235–3253.

Mitchell, J. K., L. G. Bromwell, W. D. Carrier III, N. C. Costes, W. N. Houston, and R. F. Scott (1972b), Soil-mechanics experiment in Apollo preliminary science report, *Spec. Rep. SP-289*, pp. 7-1–7-28, NASA, Greenbelt, Md.

Mitchell, J. K., W. N. Houston, W. D. Carrier, and N. C. Costes (1974), Apollo soil mechanics experiment S-200, final report, NASA contract NAS 9-11266, NASA, Washington, D. C.

Morris, R. V., R. Score, C. Dardano, and G. Heiken (1983), Handbook of lunar soils, *JSC Publ. 19069*, 914 pp., NASA Johnson Space Cent., Houston, Tex.

Nitter, T., and O. Havnes (1992), Dynamics of dust in a plasma sheath and injection of dust into the plasma sheath above moon and asteroidal surfaces, *Moon*, *56*, 7–34.

Nitter, T., T. K. Aslaksen, F. Melandsø, and O. Havnes (1994), Levitation and dynamics of a collection of dust particles in a fully ionized plasma sheath, *IEEE Trans. Plasma Sci.*, *22*, 159–172.

Nitter, T., O. Havnes, and F. Melandsø (1998), Levitation and dynamics of charged dust in the photoelectron sheath above surfaces in space, *J. Geophys. Res.*, *103*, 6605–6620.

Noble, S. K., C. M. Pieters, L. A. Taylor, R. V. Morris, C. C. Allen, D. S. McKay, and L. P. Keller (2001), The optical properties of the finest fraction of lunar soil: Implications for space weathering, *Meteorit. Planet. Sci.*, *36*, 31–42.

Papike, J., L. Taylor, and S. Simon (1991), Lunar minerals, in *Lunar Sourcebook: A User's Guide to the Moon*, edited by G. H. Heiken, D. T. Vaniman, and B. M. French, pp. 121–155, Cambridge Univ. Press, New York.

Paterson, J. L. (1992), Mobile continuous lunar excavation, engineering, construction and operations in space III, paper presented at 3rd International Conference on Engineering, Construction and Operations in Space: SPACE 92, Am. Soc. of Civ. Eng., Denver, Colo.

Pelizzari, M. A., and D. R. Criswell (1978a), Lunar dust transport by photoelectric charging at sunset, *Proc. Lunar Planet. Sci. Conf.*, *9th*, 3225–3237.

Pelizzari, M. A., and D. R. Criswell (1978b), Differential photoelectric charging of non-conductive surfaces in space, *J. Geophys. Res.*, *83*, 5233–5244.

Perkins, D. (1976), Analysis of the LEAM experiment response to charged particles, *BSR 4233*, Bendix Aerospace Syst. Div., Southfield, Mich.

Perkins, S. W. (1991), Modeling of regolith structure interaction in extraterrestrial constructed facilities, Ph. D. thesis, Univ. of Colo., Boulder.

Perkins, S. W., and C. R. Madson (1996), Mechanical and load-settlement characteristics of two lunar soil simulants, *J. Aerosp. Eng.*, *9*(1), 1–9.

Perko, H. A., J. D. Nelson, and W. Z. Sadeh (2001), Surface cleanliness effect on lunar soil shear strength, *J. Geotech. Geoenviron. Eng.*, *127*(4), 371–383.

Pieters, C., Y. Shkuratov, V. Kaydash, D. Stankevich, and L. Taylor (2006), Lunar soil characterization consortium analyses: Pyroxene and maturity estimates derived from Clementine image data, *Icarus*, *184*, 83–101.

Reasoner, D. L., and W. J. Burke (1973), Measurement of the lunar photoelectron layer in the geomagnetic tail, in *Photon and Particle Interaction With Surfaces in Space*, edited by R. J. L. Grard, pp. 369–387, Springer, New York.

Rennilson, J. J., and D. R. Criswell (1974), Surveyor observations of lunar horizon-glow, *Moon*, *10*, 121–142.

Riemann, K. U. (1995), The Bohm criterion and boundary conditions for a multicomponent system, *IEEE Trans. Plasma Sci.*, *23*, 709–716.

Riemann, K. U. (1997), The influence of collisions on the plasma sheath transition, *Phys. Plasmas*, *4*, 4158–4166.

Robertson, S., A. A. S. Gulbis, J. Colwell, and M. Horányi (2003), Dust grain charging and levitation in a weakly collisional sheath, *Phys. Plasmas*, *10*, 3874–3880.

Samir, U., K. H. Wright Jr., and N. H. Stone (1983), The expansion of a plasma into a vacuum: Basic phenomena and processes and applications to space plasma physics, *Rev. Geophys.*, *21*, 1631–1646.

Schrunk, D., B. Sharpe, B. Cooper, and M. Thangavelu (1999), *The Moon Resources, Future Development and Colonization*, John Wiley, Hoboken, N. J.

Severny, A. B., E. I. Terez, and A. M. Zvereva (1975), The measurements of sky brightness on Lunokhod-2, *Moon*, *14*, 123–128.

Sickafoose, A. A., J. E. Colwell, M. Horányi, and S. Robertson (2000), Photoelectric charging of dust particles in vacuum, *Phys. Rev. Lett.*, *84*, 6034–6037.

Sickafoose, A. A., J. E. Colwell, M. Horányi, and S. Robertson (2001), Experimental investigations on photoelectric and triboelectric charging of dust, *J. Geophys. Res.*, *106*, 8343–8356.

Sickafoose, A. A., J. E. Colwell, M. Horányi, and S. Robertson (2002), Experimental levitation of dust grains in a plasma sheath, *J. Geophys. Res.*, *107*(A11), 1408, doi:10.1029/2002JA009347.

Singer, S. F., and E. H. Walker (1962), Photoelectric screening of bodies in interplanetary space, *Icarus*, *1*, 7–12.

Sternovsky, Z., M. Horányi, and S. Robertson (2001), Charging of dust particles on surfaces, *J. Vac. Sci. Technol. A*, *19*, 2533–2541.

Sternovsky, Z., S. Robertson, A. Sickafoose, J. Colwell, and M. Horányi (2002), Contact charging of lunar and Martian dust simulants, *J. Geophys. Res.*, *107*(E11), 5105, doi:10.1029/2002JE001897.

Stubbs, T. J., R. R. Vondrak, and W. M. Farrell (2006), A dynamic fountain model for lunar dust, *Adv. Space Res.*, *37*, 59–66.

Sture, S., S. N. Batiste, M. Lankton, and J. Parisi (2004), Properties of sand under low effective stresses, paper presented at ASCE 9th Aerospace Division International Conference on Engineering, Construction and Operations in Challenging Environments, Earth and Space 2004, Am. Soc. of Civ. Eng., Houston, Tex.

Sullivan, T. A. (1994), Catalog of Apollo experiment operations, *NASA Ref. Publ. 1317*, NASA Johnson Space Cent., Houston, Tex.

Szabo, B., F. Barns, S. Sture, and H. Y. Ko (1998), Effectiveness of vibrating bulldozer and plow blades on draft force reduction, *Trans. ASAE*, *41*(2), 283–290.

Taylor, L. A., A. Patchen, D.-H. S. Taylor, J. G. Chambers, and D. S. McKay (1996), X-ray digital imaging petrography of lunar mare soils: Modal analyses of minerals and glasses, *Icarus*, *124*, 500–512.

Taylor, L. A., C. M. Pieters, L. P. Keller, R. V. Morris, and D. S. McKay (2001), Lunar mare soils: Space weathering and the major effects of surface-correlated nanophase Fe, *J. Geophys. Res.*, *106*, 27,985–27,999.

Thomas, E., Jr., A. Ivlev, A. Melzer, and W. Scales (Eds.) (2004), Special Issue on Dusty Plasmas, *IEEE Trans. Plasma Sci.*, *32*, 212 pp.

Tunaley, J. K. E., and J. Jones (1973), The photoelectron sheath around a spherical body, in *Photon and Particle Interactions With Surfaces in Space*, edited by R. J. L. Grard, pp. 59–71, Elsevier, New York.

van de Hulst, H. C. (1957), *Light Scattering by Small Particles*, Dover, Mineola, N. Y.

Vaniman, D., J. Dietrich, G. J. Taylor, and G. Heiken (1991a), Exploration, samples, and recent concepts of the Moon, in *Lunar Sourcebook: A User's Guide to the Moon*, edited by G. H. Heiken, D. T. Vaniman, and B. M. French, pp. 5–26, Cambridge Univ. Press, New York.

Vaniman, D., R. Reedy, G. Heiken, G. Olhoeft, and W. Mendell (1991b), The lunar environment, in *Lunar Sourcebook: A User's Guide to the Moon*, edited by G. H. Heiken, D. T. Vaniman, and B. M. French, pp. 51–84, Cambridge Univ. Press, New York.

Walbridge, E. (1973), Lunar photoelectron layer, *J. Geophys. Res.*, *78*, 3668–3687.

Wang, X., J. E. Colwell, M. Horányi, and S. Robertson (2007), Charge of dust on surfaces in plasma, *IEEE Trans. Plasma Sci.*, *35*, 271–279.

Weiblen, P. W., and K. Gordon (1988), Second conference on lunar bases and space activities of the 21st century, *LPI Contrib. 652*, Lunar and Planet. Inst., Houston, Tex.

Weiblen, P. W., M. J. Murawa, and K. J. Reid (1990), Preparation of simulants for lunar surface materials, paper presented at Aerospace Division of the ASCE Engineering, Construction and Operations in Space II: Space '90, Am. Soc. of Civ. Eng., Albuquerque, N. M.

Whipple, E. C. (1981), Potentials of surfaces in space, *Rep. Prog. Phys.*, *44*, 1197–1250.

Willis, R. F., M. Anderegg, B. Feuerbacher, and B. Fitton (1973), Photoemission and secondary electron emission from lunar surface material, in *Photon and Particle Interaction With Surfaces in Space*, edited by R. J. L. Grard, pp. 369–387, Springer, New York.

Willman, B. M., W. W. Boles, D. S. McKay, and C. C. Allen (1995), Properties of lunar soil simulant JSC-1, *J. Aerosp. Eng.*, *8*(2), 77–87.

Zook, H. A., and J. E. McCoy (1991), Large-scale lunar horizon glow and a high altitude lunar dust exosphere, *Geophys. Res. Lett.*, *18*, 2117–2120.

Zook, H. A., A. E. Potter, and B. L. Cooper (1995), The lunar dust exosphere and Clementine lunar horizon glow, *Lunar Planet. Sci.*, *26*, 1577–1578.

———————————

S. Batiste and M. Horányi, Laboratory for Atmospheric and Space Physics, University of Colorado, Boulder, CO 80309-0392, USA.

J. E. Colwell, Department of Physics, University of Central Florida, Orlando, FL 32816-2385, USA. (jcolwell@physics.ucf.edu)

S. Robertson, Department of Physics, University of Colorado, Boulder, CO 80309-0390, USA.

S. Sture, Department of Civil, Environmental, and Architectural Engineering, University of Colorado, Boulder, CO 80309-0428, USA.